J. Fluid Mech. (2022), *vol*. 953, A30, doi:10.1017/jfm.2022.933

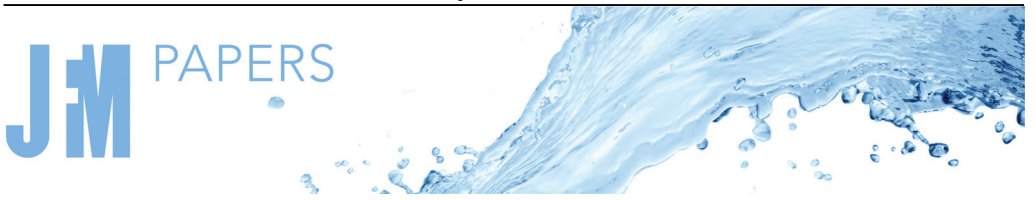

Flow instabilities and impact of ramp–isolator junction on shock–boundary-layer interactions in a supersonic intake

Nikhil Khobragade[1],†, **S. Unnikrishnan**[1] **and Rajan Kumar**[1]

[1]Department of Mechanical Engineering, FAMU-FSU College of Engineering, Florida Center for Advanced Aero-Propulsion, FL 32310 USA

(Received 15 February 2022; revised 2 October 2022; accepted 24 October 2022)

Boundary layer instabilities and shock–boundary-layer interactions (SBLIs) critically affect the performance and safe operation of mixed-compression air intakes. We present a computational study anchored in companion experiments, to evaluate the multimodal mechanisms driving the dynamics of the external compression ramp flow and the cowl SBLI in a Mach 3 intake. Boundary layer transition over the external ramp is first analysed through a global linear analysis, and the linear estimates are further validated through direct numerical simulations. The separation bubble over the ramp harbours three-dimensional stationary instabilities that induce transition, under the influence of secondary instabilities driven by the shear layer modes of the bubble. The interaction of the resulting turbulized boundary layer with the cowl shock at the ramp–isolator junction and its control through geometrical modification constitutes the second part of the study. We tested a faceted (baseline) and a notched (modified) junction design to evaluate its impact on the low-, mid- and high-frequency scales generated at the cowl SBLI region. In relation to the baseline case, the notched geometry effectively locks the separation point of the bubble, thus attenuating the upstream low-frequency breathing motion. The notch also energizes the midfrequency content through vortex shedding in a well-developed shear layer, which persists into the isolator, thus assisting in an efficient compression process through cross-stream mixing of near-wall flow. The isolator boundary layer in the notched design exhibits relatively lower static pressures and higher velocity fluctuations, which are conducive to improving the flow stability, unstart margin and efficiency of high-speed propulsion systems.

Key words: high-speed flow, compressible boundary layers, shock waves

† Email address for correspondence: nk17b@fsu.edu

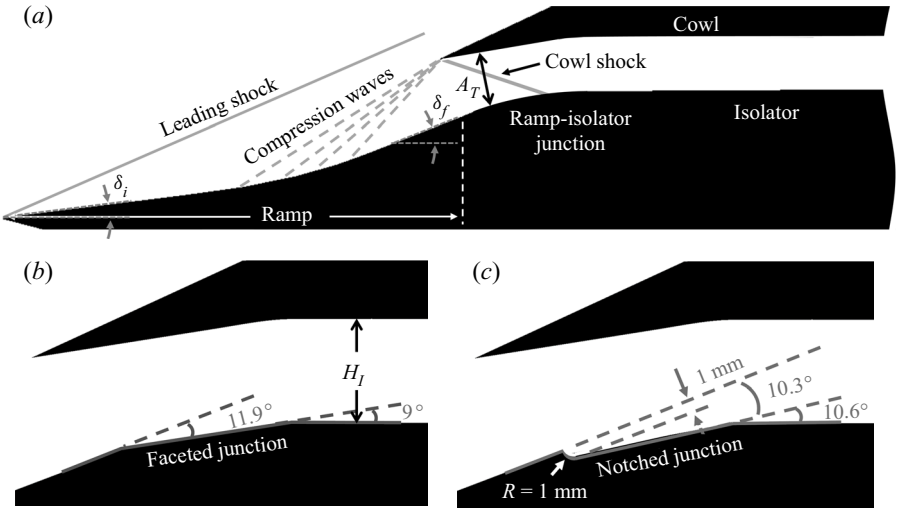

Figure 1. (*a*) Schematic of a mixed-compression intake. (*b*) Details of the baseline (faceted) junction. (*c*) Details of the modified BFS (notched) junction. Here A_T is the throat area.

1. Introduction

Mixed-compression air intakes utilize both internal and external compression for the efficient operation of a high-speed aerial vehicle (Seddon & Goldsmith 1999). The external compression occurs through a series of compressive turns designed using the method of characteristics, over the compression ramp. The internal compression occurs by geometric contraction, resulting in a series of oblique shock trains within the isolator. Losses accrued in the compression flow path can have deleterious effects on engine performance and stability of the vehicle (Oswatitsch 1980).

This work utilizes scale-resolved simulations and complementary experiments, along with constructs of hydrodynamic linear stability theory, spectral analysis and modal decomposition of multidimensional flow data, to present a fundamental study of a mixed-compression intake. The schematic in figure 1(*a*) shows the geometric elements of the mixed-compression intake, designed to operate at a free stream Mach number, $M_\infty = 3$. It includes the external compression ramp, the cowl, the ramp–isolator junction and the isolator channel. The converging compression waves and the resulting cowl shock that impinges at the junction are also schematically marked for reference. Two focus areas addressed in this work are as follows.

(i) What are the multimodal mechanisms that tailor the mean and unsteady flow features over the external compression ramp? This characterization is important due to its impact on the unsteadiness in the boundary layer ingested into the isolator, and the compression waves that coalesce into the cowl shock.

(ii) What are the dominant spatiotemporal scales in the interaction region of the cowl shock and the boundary layer in the ramp–isolator junction? How can geometrical modifications be utilized to modify this interaction in a manner that improves the robustness of the compression system?

To address the above, we first perform high-fidelity analyses of the mechanisms in the external ramp flow. These include unsteadiness induced due to adverse pressure gradients, strong surface curvatures, flow separation and shock waves. In this regard, the most

influential component of the mean flow of the ramp is the separation bubble, which dictates the effective compression profile. Depending on the streamline curvature, this region may support centrifugal (Cherubini *et al.* 2010), convective or absolute instabilities (Theofilis, Hein & Dallmann 2000). The separated two-dimensional flow is also known to harbour three-dimensional primary instabilities, often resulting in mean flow distortion and secondary instabilities (Rodríguez, Gennaro & Souza 2018). These mechanisms may induce a transition to turbulence over the ramp (Lüdeke & Sandham 2010; Zhang, Sandham & Hu 2018) if the upstream flow is laminar. The resulting turbulent boundary layer (which eventually enters the isolator) could also possess low-frequency oscillations and increased turbulence intensity, if the transition is driven by Görtler instabilities (Dolling & Murphy 1983; Tong *et al.* 2017).

The second focus area pertains to the internal compression path, which includes complexities associated with multiple shock–boundary layer interactions (SBLI) (Morgan, Duraisamy & Lele 2014) and instabilities caused due to acoustic waves (Hunt & Gamba 2019). A key interaction here is that of the cowl shock with the ramp–isolator junction. The robustness of this SBLI is critical to ensure the safe operation of the engine during off-design phenomena like inlet buzz (De Vanna *et al.* 2021) and unstart events (Wagner *et al.* 2009). It also poses safety concerns including mechanical loading due to low-frequency motions, and peak heating in strong interactions (Dolling 2001; Gaitonde 2015). Further, interaction zones affect flow separation (which determines losses and total pressure recovery), and uniformity of the flow entering the combustor. Due to the nominally two-dimensional nature of the cowl SBLI, existing studies on impinging SBLI (Adams 2000; Pirozzoli & Grasso 2006; Dupont *et al.* 2008; Piponniau *et al.* 2009) can be leveraged to understand its dynamics. However, complexities may arise here due to the unsteadiness in the impinging cowl shock, and the non-canonical nature of the junction geometry, which can induce additional inviscid features like expansion fans (Zhang *et al.* 2014).

Our analysis of cowl SBLI will be informed through prior insights into multiscale dynamics identified in canonical SBLI studies. Of specific interest is the behaviour of the low-, mid- and high-frequency components in the ramp–isolator junction. The large-amplitude low-frequency motions are typically observed at least two orders of magnitude below the scales of turbulence. They are linked with the dilation and contraction of the separation bubble and correlate with the separation shock movement (Dupont *et al.* 2008). The midfrequency component represents convective structures, signifying the shedding of coherent structures, and flapping of the separated shear layer (Agostini *et al.* 2012). High-frequency fluctuations in the interaction region often correspond to turbulent structures convected at high speeds, which result in the amplification of turbulent kinetic energy (TKE). Aubard, Gloerfelt & Robinet (2013) for example, have extracted the spatial form of these different frequency bands using Fourier analysis. All these components play a significant role in modifying the state of the postinteraction boundary layer, which determines the performance of the isolator segment.

Considering the above factors, several active and passive control techniques have been explored to manipulate SBLI in intakes. While bleed has been a frequently employed technique to remove low-momentum air and control SBLI, its implementation poses major challenges (Délery, Marvin & Reshotko 1986). Active flow control studies with microjets (Ali *et al.* 2011; Kumar *et al.* 2011; Verma & Manisankar 2012) and plasma actuators (Caraballo *et al.* 2009; Webb, Clifford & Samimy 2013) have shown promising results by reducing the amplitude of separation shock unsteadiness, and manipulation of low-frequency instability. However, active methods often result in a significant increase

in the complexity of the system. This makes the relatively simpler passive techniques an attractive alternative. Vortex generators (Valdivia *et al.* 2014; Kaushik 2019), bumps (Zhang *et al.* 2015) and streamwise slots (Holden & Babinsky 2005) are a few examples of passive techniques which have proven to be effective in SBLI control.

Motivated by its stabilizing effects in combustion chambers, the backward-facing step (BFS) geometry has also been used to passively control SBLI. Upon modifying the interaction region geometry using a BFS smaller than the incoming boundary layer thickness, Li & Liu (2019) observed that the height of the separation bubble reduces, and the reflected shock gets suppressed. An application of geometry-based SBLI control in supersonic intakes can be found in the experimental studies by Khobragade *et al.* (2020). It addresses the effects of a baseline geometry with a faceted junction, and a modified geometry with a notched junction, on unstart characteristics of a Mach 3 intake, earlier shown in figure 1(*a*). The corresponding faceted and notched junctions are presented in figure 1(*b*,*c*), respectively. The notched junction is a modification of the canonical BFS, designed to minimize distortions to the outer inviscid flow in the form of shocklets. Also, the curvature at the lower corner minimizes the secondary recirculation bubble.

Control efforts related to our second focus area will characterize the shock, bubble and shear layer dynamics of the baseline (faceted) junction, and its effect on the downstream flow that enters the isolator. The effects of the modified (notched) junction will then be presented to evaluate its utility as a control strategy for the intake SBLI. The leading edge of the notch is expected to produce a separation bubble, and the promising nature of this control strategy is supported by recent studies on shock–shear layer interactions. For example, Shi *et al.* (2021) found that the TKE increases near the interaction region and the Reynolds stress anisotropy is significantly affected. In a shock-laden cavity shear layer interaction, Karthick (2021) observed that the convection of distorting vortical structures entrain fluid mass as they convect downstream, promoting mixing.

Below, we provide the details of the experimental campaign and computational models in § 2. The external compression path is then evaluated in § 3 using global linear analysis, and direct numerical simulations (DNS). Here, we identify the dominant modes of instability, and nature of transition over the compression ramp. The flow over the ramp–isolator junction is studied in isolation, as well as in the presence of the impinging cowl shock in § 4. The impact of junction geometry is highlighted in terms of spectral and modal components of the flow field. Finally, the nature of the postinteraction boundary layer at the beginning of the isolator is analysed in § 5.

2. Methodology

The present computational analysis is informed by a complimentary experimental study of the corresponding inlet configurations, that have been previously reported in Khobragade *et al.* (2020). Selected experimental results are also utilized in this study to validate the simulations wherever possible. A brief description of the experimental campaign, details of the numerics and the computational set-up are now provided.

2.1. *Experimental campaign*

The experiments characterized the unstart phenomena in the two-dimensional mixed-compression intakes with the faceted and the notched ramp–isolator junctions, that are utilized in this work. These experiments were performed in the Polysonic Wind Tunnel at the Florida State University/Florida Center for Advanced Aero-Propulsion (FCAAP)

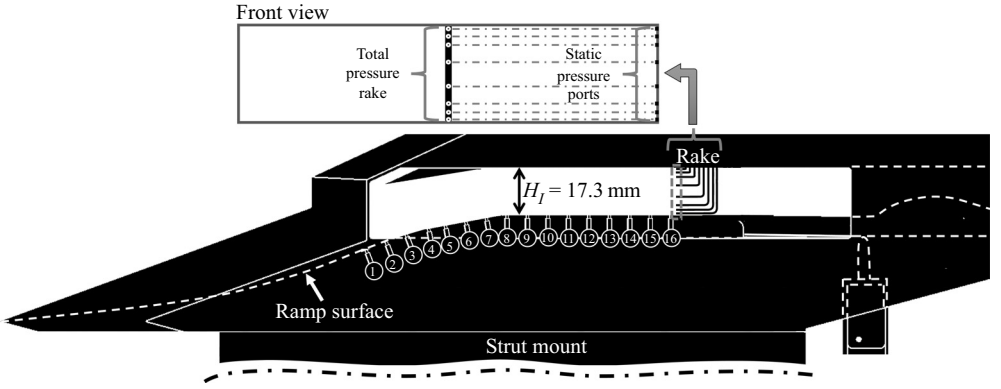

Figure 2. Schematic of a mixed-compression intake model. Bottom wall pressure ports and total pressure rake are also indicated. The inset shows a cross-section of the rake measurement plane.

(Khobragade *et al.* 2020). The incoming flow at a free stream Mach number, $M_\infty = 3$, decelerates over the compression ramp to a Mach number of approximately 2.1. This flow enters the ramp–isolator junction, where the cowl shock interacts with the incoming turbulent boundary layer. The Reynolds number is $Re \sim 4.1 \times 10^5$, based on the free stream parameters, and the isolator height ($H_I = 17.3$ mm). The ramp is designed with an initial wedge angle of $\delta_i = 6.7^\circ$, and a final angle of $\delta_f = 20.8^\circ$. The isolator duct is 90 mm (3.55 in.) long and has a cross-section of 75 mm $\times$ 17.34 mm (Aspect Ratio = 4.3), corresponding to a cross-sectional area of 1301 mm^2. A schematic of the intake model is shown in figure 2.

The ramp–isolator part of the intake has 16 ports (E1 to E16) distributed along the streamwise direction to measure the centreline static pressures on the bottom wall (figure 2). To obtain the Mach number and total pressure, a combination of an eight-probe Pitot rake and sidewall static pressure ports was used. The plane of rake measurement is located at a streamwise distance of $14.4H_I$ from the origin. The port-side wall has eight pressure ports at the rake measurement plane which are vertically aligned with the total pressure probe heads as shown in the inset of figure 2. The current experimental set-up has a provision to record up to 16 channels of steady pressure data using an electronic differential pressure scanner (ESP-16HD), which has a range of $\pm$207 kPa ($\pm$30 psi). The bottom wall pressures, rake pressures and sidewall pressures were recorded using this scanner at a frequency of 30 Hz. The pressure scanner has a maximum error of $\pm$0.03 % of full-scale pressure. This corresponds to the maximum uncertainty of $\pm$62 Pa in centreline pressure and $\pm$0.0006 in non-dimensionalized pressure. These uncertainties apply to the total pressures measured using the rake and corresponding sidewall static pressures. The uncertainty in the centreline Mach number is $\pm$0.001. The uncertainty in the centreline total pressure recovery, which is the measured centreline stagnation pressure normalized by the free stream stagnation pressure, is $\pm$0.03 %.

The flow field was visualized using a conventional Z-type shadowgraph set-up consisting of two 0.4128 m-diameter parabolic mirrors of 2 m focal length aligned on either side of the test section. For illumination, a light-emitting diode was utilized as a light source that focused light on the rectangular slit through an achromatic lens. The shadowgraph images were recorded at a rate of 2 kHz with a Phantom V411 (Vision Research) high-speed camera.

2.2. *Direct numerical simulation*

The DNS solves three-dimensional time-dependent compressible Navier–Stokes equations in the generalized curvilinear coordinates, cast in the strong conservation form. The system of equations (Vinokur 1974; Anderson, Tannehill & Pletcher 1984) is given as

$$\frac{\partial}{\partial \tau}\left(\frac{\boldsymbol{Q}}{J}\right) = -\left(\frac{\partial \boldsymbol{F_i}}{\partial \xi} + \frac{\partial \boldsymbol{G_i}}{\partial \eta} + \frac{\partial \boldsymbol{H_i}}{\partial \zeta}\right) + \frac{1}{Re}\left(\frac{\partial \boldsymbol{F_v}}{\partial \xi} + \frac{\partial \boldsymbol{G_v}}{\partial \eta} + \frac{\partial \boldsymbol{H_v}}{\partial \zeta}\right). \tag{2.1}$$

Here $\boldsymbol{Q} = [\rho, \rho u, \rho v, \rho w, \rho E]^{\mathrm{T}}$ represents a vector of conserved variables; (u, v, w) are the Cartesian components of velocity along the directions, (x, y, z); ρ is the density; $E = T/(\gamma(\gamma - 1)M_\infty{}^2) + (u^2 + v^2 + w^2)/2$ denotes total specific internal energy; M_∞, T and γ represent the reference free stream Mach number, temperature, and the ratio of specific heats, respectively. The ideal gas law, $p = \rho T/\gamma M_\infty{}^2$, is used, where p is pressure. The length and velocity scales used for normalization are the isolator height, H_I, and free stream velocity, U_∞, respectively. The density and temperature have been normalized by their respective free stream values, while pressure has been non-dimensionalized by $\rho_\infty U_\infty{}^2$. The Jacobian of the coordinate transformation is given by $J = \partial(\xi, \eta, \zeta, \tau)/\partial(x, y, z, t)$. Here (ξ, η, ζ) represent the curvilinear coordinates, $(\boldsymbol{F_i}, \boldsymbol{G_i}, \boldsymbol{H_i})$ are the inviscid fluxes and $(\boldsymbol{F_v}, \boldsymbol{G_v}, \boldsymbol{H_v})$ are the corresponding viscous fluxes (Garmann 2013). Here Re is the Reynolds number, based on the free stream parameters, and the isolator height. In the following discussion, non-dimensional frequency, Strouhal number (St), is based on H_I and U_∞. A constant Prandtl number, $Pr = 0.72$, is assumed for air, with $\gamma = 1.4$. Temperature dependence of viscosity is modelled using Sutherland's formula with a reference temperature of 224 K and Sutherland's constant as 110.33 K.

The DNS implements a high-order approach, utilizing the seventh-order WENO (weighted essentially non-oscillatory) (Balsara & Shu 2000) scheme for reconstruction, and the Roe scheme (Roe 1981) for evaluation of inviscid fluxes. To minimize oscillatory behaviour in the vicinity of shocks (Bhagatwala & Lele 2009), a third-order upwind scheme along with the van Leer harmonic limiter (van Leer 1979) is adopted. Fourth-order central difference is used to discretize the viscous terms, and time-integration is performed through the second-order diagonalized (Pulliam & Chaussee 1981) implicit Beam–Warming method (Beam & Warming 1978). An explicit approach (Shu & Osher 1988) was also utilized to ensure that the mean and unsteady features of the flow fields are not sensitive to the choice of the time-integration scheme. The DNS solver has been validated and applied to boundary layer and inlet-related problems in prior publications (Unnikrishnan & Gaitonde 2020; Khobragade, Unnikrishnan & Kumar 2021).

To ensure the feasibility of the computational cost associated with the near-wall resolution, the Reynolds number in the DNS ($Re = 40\,000$) is one order of magnitude lower than that in the experiments. For inlet-related studies, this approach enables the utilization of high-fidelity simulations to study relevant physical phenomena with adequate accuracy, as demonstrated in Morgan *et al.* (2014). Although some differences exist, we expect the DNS Reynolds number to be sufficiently high to generate meaningful physical insights into the experimental conditions, due to the robustness of unsteady flow features across Reynolds numbers (Souverein *et al.* 2010) in this regime.

To reconcile the inferences from the DNS predictions and experimental results, where appropriate, we also include predictions from Reynolds averaged Navier–Stokes (RANS) simulations, which are performed at the experimental Re. The RANS equations solve the two-dimensional form of (2.1), with the above-mentioned third-order approach throughout the domain. Turbulence modelling is implemented using the K–ϵ model, where K is the

TKE, and ϵ is the turbulent dissipation rate. Details of the RANS formulation can be obtained from Gerolymos (1990) and Rizzetta & Visbal (1993).

2.3. *Linear stability analysis*

Linear stability analysis (LSA) facilitates insightful interpretations of the DNS results, highlighting linear mechanisms that constitute fundamental characteristics of the basic state. Traditional operator-based LSA can be challenging while applying to non-homogeneous compressible flows, due to the complexity of the explicit linear operator. To circumvent this, we adopt a matrix-free approach, termed 'Navier–Stokes-based mean flow perturbation' (NS-MFP), to extract the linear response of the laminar flow relevant to the inlet configuration analysed here. The NS-MFP is an augmented version of the body-force constrained implicit linearization approach reported by Touber & Sandham (2009) in the study of two-dimensional SBLI. Detailed validation and application of NS-MFP to a variety of flows harbouring convective and absolute instabilities are reported in prior works (Ranjan, Unnikrishnan & Gaitonde 2020; Ranjan *et al.* 2021; Unnikrishnan & Gaitonde 2021) and references therein.

The matrix-free paradigm is particularly useful to handle applications in generalized curvilinear coordinates and also leverages the high-order formulation available in the Navier–Stokes solver. For the current work, NS-MFP utilizes a sixth-order compact-difference scheme along with an eighth-order filter, with $\alpha = 0.45$ (Visbal & Gaitonde 1998), to discretize the convective fluxes. Viscous fluxes are discretized using the second-order central difference. Time integration is implemented using the nonlinearly stable third-order Runge–Kutta scheme (Shu & Osher 1988). To ensure fast convergence of the instability modes, the Krylov subspace vectors obtained from NS-MFP are orthogonalized through the Arnoldi-based approach, commonly utilized in 'time stepper' techniques (Bagheri *et al.* 2009).

2.4. *Flow configurations studied*

The current study focuses on the dynamics of the flow over the external compression ramp, and the leading SBLI with the cowl shock. To systematically identify the impact of geometrical features on the flow, we choose four different flow configurations for the DNS study, as shown in figure 3. This includes the ramp-only configurations (ROCs) of the faceted (figure 3*a*) and notched (figure 3*c*) junctions, that will be utilized to study the basic variations induced by the junction geometry in the turbulized boundary layer entering the isolator. In addition, we also simulate the effects of the cowl-side wall for these respective cases, as shown in figure 3(*b*,*d*).

The DNS recreates the tunnel conditions of 0.1 % free stream turbulence intensity by prescribing synthetic turbulence (Adler *et al.* 2018) at the inlet of the computational domain, on a uniform background flow field. Subsequently, a boundary layer develops over the ramp and undergoes a transition to turbulence. The walls are treated as adiabatic no-slip surfaces over the ramp. Supersonic outflow conditions are applied on the outflow (right-hand boundary). Periodic conditions are imposed in the spanwise direction. Over the cowl wall, adiabatic no-slip conditions are enforced within the streamwise range, $x_{LEC} \leq x \leq x_{LEC} + 0.6$, where x_{LEC} is the leading edge of the cowl. This region is marked between two arrows in figure 3(*b*,*d*), and was found sufficient to ensure complete reflection of the converging compression waves (emanating from the ramp) into the cowl shock (towards the ramp–isolator junction). The rest of the cowl wall is treated as an outflow. This approach was adopted to reduce the wall-resolution requirements in the DNS for the

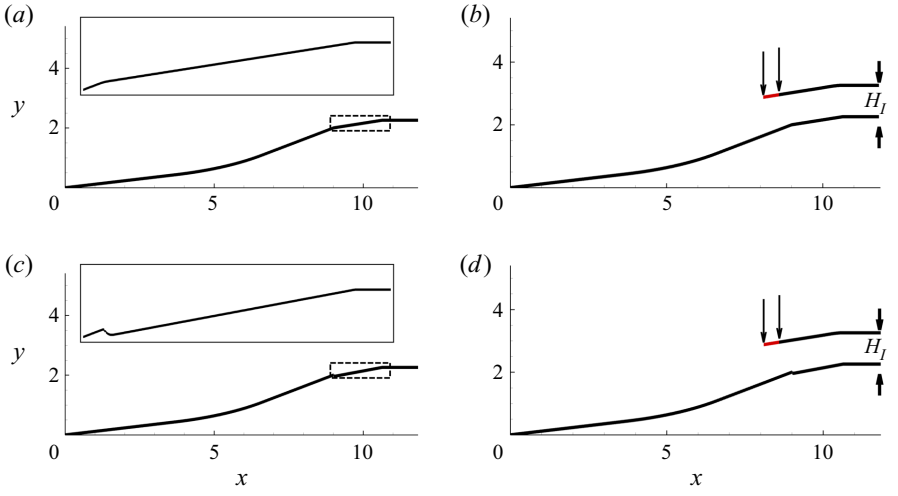

Figure 3. Ramp-only configurations of the (*a*) faceted and (*c*) notched junction designs. Cowl-side wall included in the (*b*) faceted and (*d*) notched junction designs. The junction geometries are magnified for clarity in the insets in (*a*,*c*). The vertical arrows in (*b*,*d*) mark the no-slip adiabatic wall simulated on the cowl-side.

cowl surface since the primary features studied here are the SBLI over the ramp–isolator junction, and the boundary layer immediately downstream of it.

A preliminary analysis of the ROC reported in Khobragade *et al.* (2021) addresses various computational requirements for this flow, including grid resolution, inflow turbulence generation parameters and spanwise extent. The grids utilized for the current simulations have a wall-normal spacing, $\Delta n_W = 5 \times 10^{-4} H_I$, over the ramp-side wall, corresponding to the finer grid adopted in the above study. Since only the leading edge of the cowl-side wall is incorporated, the wall resolution here is relatively coarse, with $\Delta n_W = 1 \times 10^{-2} H_I$. The computational domain spans $0 \leq x \leq 11.8$, $0 \leq y \leq 3.26$ and $-0.2 \leq z \leq 0.2$, with the origin at the leading edge of the compression ramp. The spanwise extent of the grid is chosen to be around six times the peak spanwise integral length scale over the notched ROC, as reported in Khobragade *et al.* (2021). In the turbulized region of the ramp ($x \sim 8.5$), the DNS mesh resolution in wall units is $\Delta x^+ \sim 6.9$, $\Delta y^+ \sim 0.77$ and $\Delta z^+ \sim 4.1$. Based on a grid resolution study, these parameters were found to adequately resolve the boundary layer. The grid is discretized uniformly in the spanwise direction. The RANS calculations are performed on a grid with relatively finer wall-normal spacing, $\Delta n_W = 1 \times 10^{-4} H_I$.

3. Compression ramp flow characteristics

The external flow development over the compression ramp and the associated boundary layer dynamics are studied in the context of fundamental linear instabilities. Its effects on spatiotemporal scales induced in the transitional and turbulent zones that develop prior to the cowl shock interaction are then obtained using a DNS.

3.1. *Linear dynamics of ramp flow*

The temporal linear stability analysis is performed on the laminar basic state, obtained by solving the two-dimensional form of (2.1). The resulting flow field at $M_\infty = 3$, and

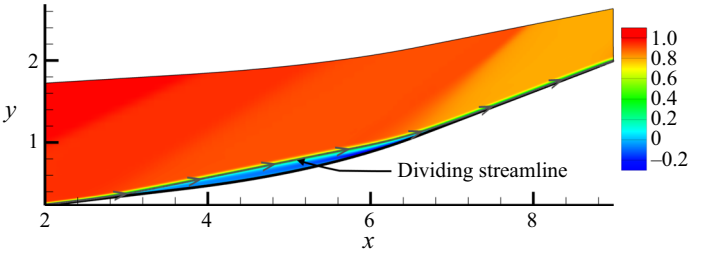

Figure 4. Laminar flow field over the compression ramp utilized for stability analysis. Streamwise velocity contours are shown along with the dividing streamline that delineates the separation bubble.

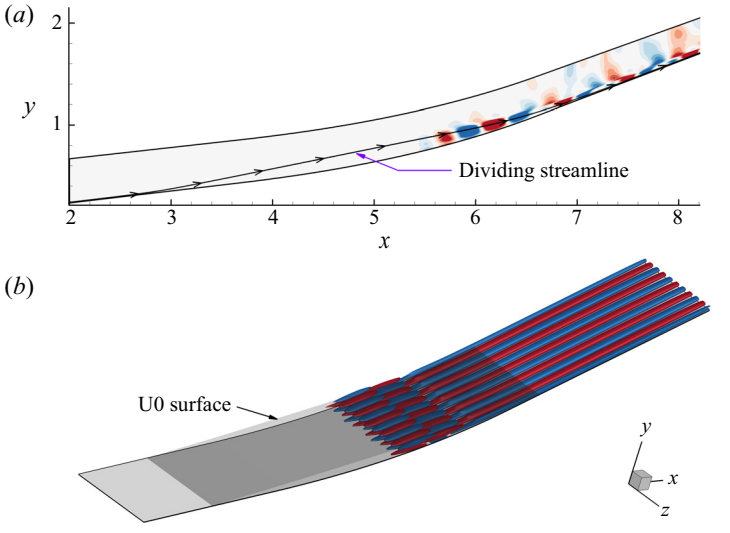

Figure 5. Instability modes over the compression ramp. (*a*) Two-dimensional shear layer mode identified using contours of streamwise velocity. (*b*) Three-dimensional stationary mode identified using isolevels of streamwise velocity. The U0 surface in panel (*b*) is the spanwise-extruded surface corresponding to the dividing streamline shown in panel (*a*). Here (*a*) $St \sim 1.8$, GR ~ -0.1; (*b*) $St = 0$, GR ~ 0.07.

$Re = 40\,000$, is shown in figure 4. The isentropic compression corner exists approximately within $3.8 \leq x \leq 6.6$. As clearly visible in figure 4, a separation bubble forms over the compression ramp, spanning $2.9 \leq x \leq 7.0$. The flow separation is a result of the adverse pressure gradient imposed by the compression waves, and its extent propagates upstream due to the laminar state of the near-wall flow. The maximum displacement thickness of the separated shear layer over the bubble is $\sim$0.133, at $x \sim 5$. The maximum reversed flow exists at $x \sim 5.84$, at a wall-normal distance of 0.022, with the corresponding value, $u = -0.22$.

The linear analysis identified convective and absolute instabilities over the compression ramp, the most significant of which are reported in figure 5. The results are reported in terms of the real and imaginary components of the eigenvalues ($\omega = \omega_R + i\omega_I$) of the Jacobian matrix that represents the laminar basic state. Here, ω_R is the temporal growth rate (GR) of the instability, and ω_I is its non-dimensional circular frequency. For the convenience of comparison with DNS results in the following sections, the instability frequencies are converted into St ($St = \omega_I/(2\pi)$).

A characteristic feature of the separated shear layer is the two-dimensional Kelvin–Helmholtz (KH) instability modes generated within the inflectional velocity profile. The least-damped mode from the time stepper analysis was identified to be at a non-dimensional frequency, $St \sim 1.8$, with a negative growth rate, $GR \sim -0.1$. Figure 5(*a*) shows the spatial form of this two-dimensional shear layer mode using contours of streamwise velocity fluctuations. The separated shear layer amplifies the instability in the downstream direction, towards the maximum displacement position. The oscillation frequency of KH mode when scaled with the momentum thickness at the upstream end of the bubble is $St_\theta \sim 0.0135$. This lies in the range of KH instability frequencies observed in other laminar separation bubble studies ($0.0069 \leq St_\theta \leq 0.017$), e.g. Pauley, Moin & Reynolds (1990), Watmuff (1999) and Kurelek, Lambert & Yarusevych (2016). The convective instability is attenuated postreattachment but continues to exist at lower amplitudes at downstream locations over the ramp, indicating its potential role in tailoring the flow ingested into the inlet.

With respect to the edge velocity of 0.95 at the upstream end of the separation bubble, the peak reverse velocity in the bubble is 23.6 %. Such magnitudes of peak reverse velocity may result in an absolute instability within the separation bubble, as shown in stability analyses by Huerre & Monkewitz (1985) and Alam & Sandham (2000). Studies by Theofilis *et al.* (2000) on incompressible laminar boundary layer also indicate that instabilities of the separation bubble could be induced by travelling as well as non-travelling (stationary) modes. The current linear analysis identifies such a zero-frequency mode to possess a positive growth rate, indicating the presence of absolute instability over the ramp. Figure 5(*b*) shows this three-dimensional stationary mode on the compression ramp, using isosurfaces of streamwise velocity fluctuations. It has a harmonic structure in the spanwise direction with a spanwise wavelength, $\lambda_z \sim 0.2$. This mode exhibits a positive growth rate, $GR \sim 0.07$, as expected from an absolute instability, and has the potential to induce flow transition over the compression ramp. Rodriguez & Theofilis (2010) have observed similar flow structures with spanwise periodicity to exist in laminar separation bubbles. Such structures manifest as streamwise-oriented counter-rotating swirling regions near the wall. More recently, Hildebrand *et al.* (2018) also observed a similar stationary mode around the separation bubble in hypersonic SBLI. They found that elongated streamwise structures of this mode are coupled with the shear layer on top of the recirculation bubble. The presence of these multiple instabilities leads to intermodal interactions in the nonlinear flow field, that influence the state of the incoming boundary layer in the isolator, and will be explored in the following sections using DNS.

3.2. *Direct numerical simulation of ramp flow*

Here, we present the nonlinear characteristics of the external flow over the compression ramp using a DNS. For an overall description of this flow field, figure 6 shows the flow features captured by the DNS using an isolevel of Q-criterion, coloured by streamwise velocity. The flow behaviour in the vicinity of the compression curvature is magnified in the inset, which identifies the transition to turbulence downstream of the reattachment point over the ramp. Incoming perturbations induce fine-scale vortical structures in the upstream boundary layer, which develop spatiotemporal coherence after convecting downstream. Once the boundary layer separates, predominantly two-dimensional rollers appear in the shear layer. Hosseinverdi & Fasel (2019) have observed similar rollers in laminar separation bubbles, which result from the KH instability mechanism. These rollers consist of two-dimensional (major) and oblique (minor) structures. As identified in the

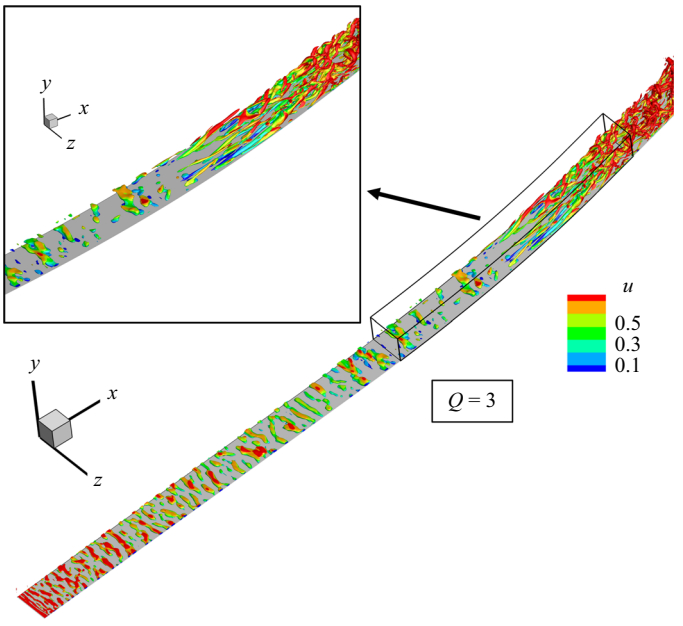

Figure 6. Flow structures in the compression ramp boundary layer identified using isolevel of Q-criterion, coloured with u-velocity. The inset shows a magnified flow field within the indicated regions of interest.

linear analysis above, the two-dimensional KH mode exhibits a relatively higher rate of amplification (although slightly damped), thereby making it more influential in shaping the nonlinear response. However, the amplification of weakly oblique three-dimensional disturbances is also captured in the DNS (as indicated by the presence of oblique coherent structures), since the synthetic turbulence imposed at the inflow plane includes a broad range of spanwise wavenumbers. Downstream of the rollers, streamwise streaky structures appear after reattachment. It is typical to observe such streamwise structures within laminar separation bubbles, and they could be induced due to various instability mechanisms such as Klebanoff modes (Hosseinverdi & Fasel 2019) or centrifugal modes (Cherubini *et al.* 2010). Yao *et al.* (2007) identified an absolute instability that drives the streamwise vortex patterns at the rear of the bubble. As seen in figure 6, the streaky structures generate hairpin vortices and eventually disintegrate into turbulent structures spanning a wide range of length scales. Krishnan, Sandham & Steelant (2009) reported a similar transition to turbulence on the cowl-side compression ramp. Teramoto (2005) showed that such a transition process is self-sustained and is independent of the upstream disturbances. A boundary layer turbulized in this way enters the ramp–isolator junction on the floor of the inlet.

The time-averaged streamwise velocity field of the compression ramp obtained from the DNS is shown in figure 7. Boundary layer profiles (based on tangential velocity component) at several streamwise locations are also displayed in the insets. The amplification of three-dimensional instabilities in the DNS leads to boundary layer transition, making it fully turbulent by the end of the ramp. A major impact of this on the time-averaged flow is that the DNS recirculation zone is smaller when compared with that of the laminar case. With separation and reattachment points at $x \sim 3.9$, and $x \sim 5.84$, respectively, the DNS separation bubble is approximately 2 units long in streamwise extent, which is ∼47 % of the streamwise length of separation bubble in the laminar flow.

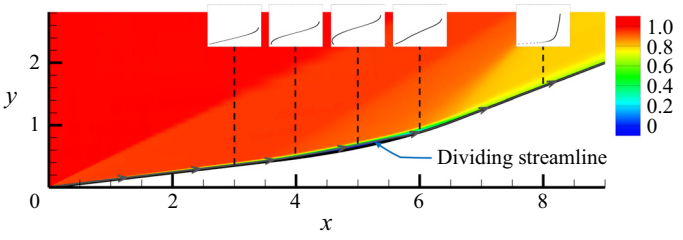

Figure 7. Streamwise velocity contours from the time-averaged DNS over the compression ramp. The evolution of velocity profiles along the ramp is also shown.

The maximum displacement thickness over the bubble is 0.047, which occurs at $x \sim 5$, and the peak reversed flow velocity is 3.1 %. The presence of incoming flow turbulence in the DNS leads to significant cross-stream velocity fluctuations penetrating into the separating boundary layer, which can also reduce bubble length and height. These results are in accordance with the studies on the effect of free stream turbulence on the properties of laminar separation bubbles, by Simoni *et al.* (2017). The boundary layer over the ramp is impacted by an adverse pressure gradient on the isentropic compression surface, as the static pressure increases along the ramp. The evolution of this boundary layer in figure 7 identifies a laminar profile at the beginning of the ramp, a separated profile in the middle, reattached profile downstream, and a fuller profile characteristic of turbulent flow towards the end of the ramp. The boundary layer profile exhibits an inflection point prior to the flow separation (not displayed), a characteristic of flow developing in an adverse pressure gradient. The final state of the ramp boundary layer is further quantified below.

It is important to fully characterize the ramp boundary layer entering the inlet due to its influence on the cowl SBLI, and the flow inside the isolator. Here we report the velocity statistics of the boundary layer at the end of the ramp ($x \sim 8.5$). The mean profile of the velocity tangential to the ramp surface is plotted using wall units, u^+ and y^+, and is shown in figure 8(a). To account for the compressibility effects, Trettel–Larsson transformation (Trettel & Larsson 2016) is applied to obtain the transformed velocity, u^+_{TL}. The linear relation between u^+_{TL} and y^+, a characteristic of the viscous sublayer, is evident until $y^+ \sim 7$. The mean velocity profile shows a good match with the log-layer reference line for $y^+ > 20$, indicating the fully developed turbulent state of the boundary layer. To characterize the dynamical nature of the boundary layer at this location, the one-dimensional energy spectrum is generated and shown in figure 8(b). The spectrum confirms the presence of a well-developed inertial subrange with a $St^{-5/3}$ slope, and the dissipation range with a St^{-7} roll-off. Thus, an equilibrium cascade process is established by the end of the ramp following a transition to turbulence in the middle.

The dynamics of the compression ramp flow is now evaluated using spectral and modal analysis of the DNS, in the context of its linear properties (§ 3.1). Figure 9 shows the spectrum of wall-pressure fluctuations with the separation and reattachment locations marked using black dashed lines. A dominant component of energy that emerges within the ramp separation zone corresponds to the convectively unstable KH waves ($1.7 \leq St \leq 3$), which are observed as spanwise rollers in figure 6. This KH band also includes the shear layer instability frequency predicted by the linear analysis, seen earlier in figure 5. When scaled with the momentum thickness at the onset of separation, the KH band spans $0.0156 \leq St_\theta \leq 0.0275$, which overlaps with the range of frequencies observed in other studies (Kurelek *et al.* 2016; Simoni *et al.* 2017), with the excitation of additional higher frequencies. Figure 9 also identifies a set of lower frequencies, $0.1 \leq St \leq 0.3$ ($0.0067 \leq$

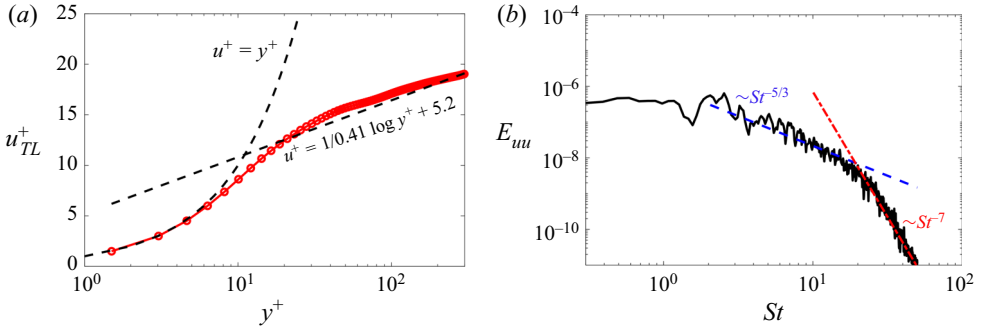

Figure 8. (*a*) Tangential velocity profile at the ramp-end at $x = 8.5$, plotted using wall units. Reference curves for the viscous sublayer and log-layer are also included. (*b*) One-dimensional energy spectra calculated from streamwise velocity fluctuations at $x = 8.5 \times St^{-5/3}$ and St^{-7} lines are also indicated.

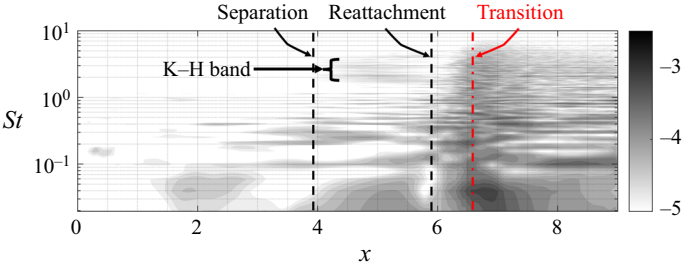

Figure 9. Wall-pressure spectra (log–PSD) of the compression ramp flow. Separation, reattachment, transition locations and KH mode frequency band are indicated.

$St_\delta \leq 0.02$), that are prominent upstream of the separation, and further amplify within the separation zone. Priebe & Martín (2012) found a similar range of frequencies when scaled with the boundary layer thickness, δ. These are perhaps the characteristic frequencies of the incoming boundary layer which get amplified by the shear layer instability. The very low frequencies ($St \leq 0.1$) prior to separation are oblique in nature, most likely driven by the instabilities of the boundary layer.

While the unsteadiness due to KH instabilities attenuates postreattachment, high amplitude oscillations emerge over a wide range of lower frequencies. A relevant candidate mechanism here for boundary layer transition is Görtler vortices, and their secondary instabilities. To evaluate the viability of this mechanism, the Görtler number (G_t) is calculated using the radius of curvature of the dividing streamline and mean flow boundary layer thickness. The Görtler Number is defined as, $G_t = (U_\infty \delta/\nu)(\delta/R)^{1/2}$, where U_∞ denotes free stream velocity, δ is the boundary layer thickness, ν is the kinematic viscosity and R is the radius of curvature of the dividing streamline. Based on linear theory, centrifugal instability due to the wall curvature destabilizes the flow for $G_t > 0.46$, and experiments show that disturbances amplify for Görtler numbers of the order of few 10s (Floryan 1991). In this study, the Görtler number was found to be sufficiently high (~ 900) near the reattachment point ($x \sim 6$), which suggests the possibility of the emergence of Görtler vortices. Therefore, the low-frequency unsteadiness in the vicinity of reattachment is most probably driven by the Görtler instability, resulting in the appearance of quasistationary streamwise vortices near the wall. These vortices are evident as streaky structures in the Q-criterion isolevel visualization of the DNS (figure 6).

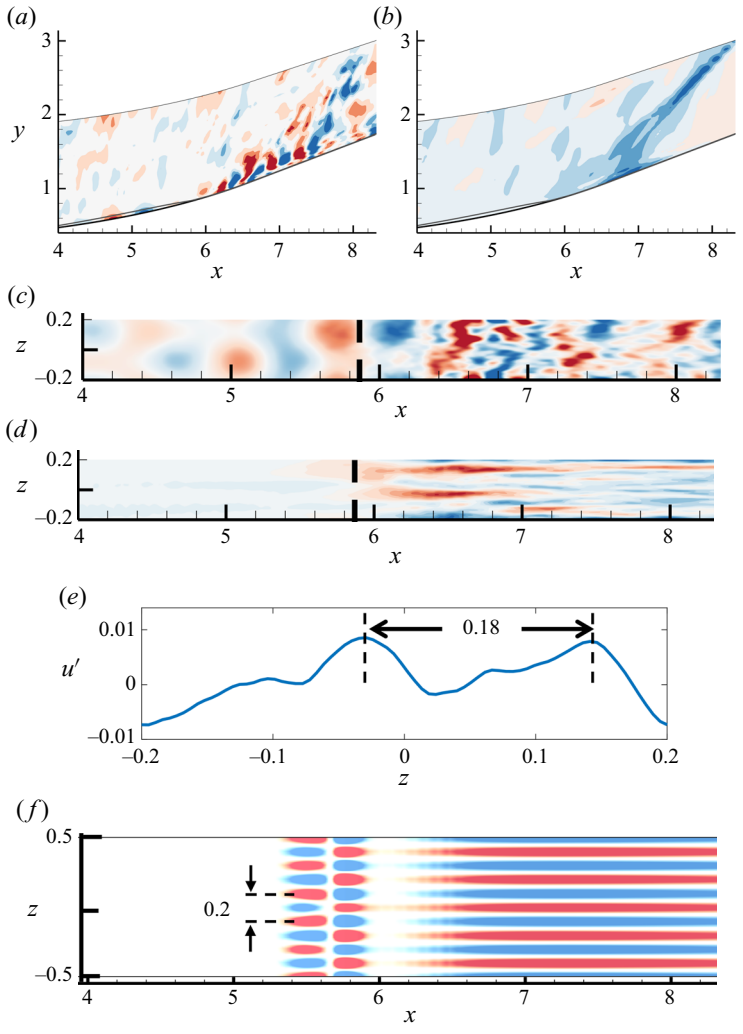

Figure 10. The DMD modes extracted over the ramp from the DNS. (*a*,*b*) Pressure modes on the midspan plane. (*c*) Pressure mode on the wall-parallel surface. (*d*) The u-velocity mode on the wall-parallel surface. (*e*) Spanwise distribution of streamwise velocity of '$St \sim 0.036$' dynamic mode decomposition (DMD) mode. (*f*) Wall-parallel slice of the stationary mode from linear analysis. The dashed lines indicate reattachment locations in panels (*c*,*d*). Dividing streamlines are indicated in the midspan contours. Here (*a*) $St \sim 1.75$ (p); (*b*) $St \sim 0.037$ (p); (*c*) $St \sim 1.81$ (p); (*d*) $St \sim 0.036$ (u); (*e*) $St \sim 0.036$ (u) at $x \sim 6.5$; (*f*) $St = 0.0$ (u-MFP).

The destabilization of these structures through the generation of hairpin vortices energizes a broad spectral range downstream of reattachment. The broadband nature of the pressure spectrum towards the end of the ramp reaffirms the turbulized nature of the boundary layer.

The inferences from the preceding spectral characterization are further elaborated using the modal analysis of pressure and velocity perturbations over the compression ramp in figure 10. The spatiotemporal characteristics of the nonlinear flow field are obtained using DMD (Schmid 2010), which is applied to the pressure and streamwise velocity fluctuations provided by the DNS. This analysis is focused on the region of the compression ramp where the boundary layer undergoes a transition.

Midspan features of two relevant pressure modes are presented in figure 10(*a*,*b*). The spatial support of the mode corresponding to $St \sim 1.75$ shows initial amplification of separated shear layer perturbations around the location of maximum displacement thickness ($x \sim 5$). It corresponds to the two-dimensional KH instability identified in the linear analysis in figure 5(*a*). The mode further shows amplified unsteadiness in the outer boundary layer, post reattachment ($x > 6$), where the transition to turbulence takes place. This is the signature of the horseshoe vortices developing over the quasistationary Görtler instabilities. Li & Malik (1995) have described this mode as an even or varicose instability in which the Görtler vortices develop into horseshoe-type structures and eventually disintegrate into turbulence. Thus, we identify the role of KH instabilities within the ramp separation zone in driving the secondary instabilities of Görtler vortices, resulting in the turbulent breakdown of the boundary layer. The spatial support of the low-frequency mode ($St \sim 0.037$) in figure 10(*b*) shows amplification of perturbations in the transition zone ($x \sim 6.5$), which is consistent with the DNS power spectral density (PSD) plot in figure 9. It is important to note that these unsteady features resulting from the transition dynamics of the ramp boundary layer, propagate through the ramp shock towards the cowl lip. This has implications for shock-on-lip operating conditions, that are critical for the efficient operation of the engine (Seddon & Goldsmith 1999).

Near-wall dynamics represented by these modes are explored using the second set of DMD analyses, using pressure and velocity data adjacent to the wall. Relevant modes are presented using pressure (figure 10*c*) and streamwise velocity (figure 10*d*) spatial supports. The $St \sim 1.81$ mode corresponding to the KH band of frequencies shows amplification of a nearly two-dimensional instability within the bubble. This is the signature of the spanwise rollers, as seen on the wall surface. Similar to the midspan mode (figure 10*a*), the wall-parallel mode shows enhanced perturbations post reattachment due to the secondary instability of Görtler vortices. As shown in figure 10(*d*), the signature of Görtler vortices appear as streamwise structures in the low-frequency mode, in the vicinity of the reattachment point. Spectral analysis of this mode reveals that the spanwise wavenumber around the reattachment region ($6.2 \leq x \leq 6.8$) is, $k_z \sim 4.93$, which corresponds to a spanwise wavelength of, $\lambda_z \sim 0.203$. For instance, figure 10(*e*) marks the peak-to-peak distance in the spanwise profile of the low-frequency DMD mode extracted at $x \sim 6.5$, which has a value of 0.18. For the convenience of comparison, a top view of the wall-parallel slice of the stationary mode extracted using the linear analysis is shown in figure 10(*f*). The wavelength of the low-frequency mode extracted from DNS shows a good match with that of the stationary mode predicted by linear theory.

4. Cowl shock and ramp boundary layer interactions

The compression waves produced by the ramp are directed towards the cowl lip and are reflected as a cowl shock towards the ramp–isolator junction. We now present the simulations that study this phenomenon, by accounting for the leading edge of the cowl.

Basic characteristics of the flow field can be understood by evaluating the time-averaged field in the baseline faceted junction. This is presented in figure 11 using the second derivative of density, to highlight the boundary layer and inviscid features. The solid wall that produces the cowl shock is shown as a red line on the top surface. While the flow turns away from the intake axis or the streamwise direction over the compression ramp, it turns back towards the streamwise direction around the ramp–isolator junction. Complex interactions occur in the vicinity of the junction due to the presence of shocks, expansion fans, flow separation, boundary layers and shear layers. Eventually, the mean flow becomes

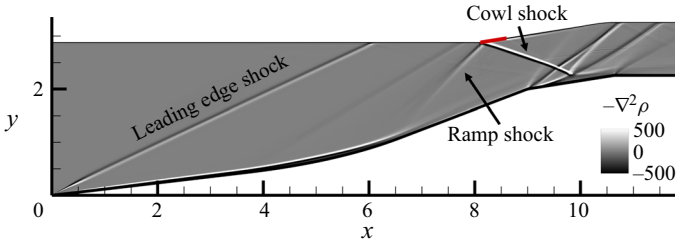

Figure 11. Numerical shadowgraph of the full flow field with the cowl SBLI at the faceted junction.

parallel to the streamwise direction in the isolator, through an expansion fan at the isolator entrance.

The previous section identified a turbulent boundary layer at the isolator entrance, over the ramp-side wall. In addition to this intake floor unsteadiness, the compression ramp also influences the unsteadiness over the internal surface of the cowl. The ramp shock originates in the region where the flow transitions over the ramp ($x \sim 7$). As shown earlier in the midplane pressure modes (figure 10*a*,*b*), the ramp shock is directly affected by the ramp flow instabilities and guides the corresponding oscillations towards the cowl lip. Thus, ramp unsteadiness has a two-fold effect on the dynamics at the inlet entrance (on the ramp-side and cowl-side walls). These aspects will be quantitatively analysed in the following discussion, with special emphasis on the role of junction geometry in modifying the interaction region.

4.1. *Ramp–isolator junction flow fields*

The four DNS utilized to study the flow in the ramp–isolator junction are visualized in figure 12, using an isolevel of Q-criterion, coloured by streamwise velocity. The ROCs of the faceted and notched junctions are shown in figure 12(*a*,*c*), respectively. The cowl SBLIs in the corresponding cases are shown in figure 12(*b*,*d*), respectively, using density-gradient contours on a spanwise plane. The two geometries exhibit key differences in several aspects of the flow, including, unsteady scales in the boundary layer, size of the separation bubble, structure of separation-induced compression waves emanating from the junction, and postinteraction boundary layer.

The mean flow fields of these four cases are compared in figure 13. The $\boldsymbol{u} \cdot \boldsymbol{\nabla} p$ fields are utilized to effectively identify the compression and expansion zones, which appear as the red and blue fields, respectively. Streamlines are also included to indicate the turning of the flow due to these waves. The compression ramp shock is visible at the top left-hand corners. In the faceted ROC (figure 13*a*), the scenario is relatively simpler, where the flow turns towards the streamwise direction through two expansion fans. The notched ROC (figure 13*c*) displays a comparatively stronger expansion fan at the step edge, followed by a reattachment shock. Although not marked, a localized recirculation bubble exists between the expansion fan and reattachment shock.

The cowl SBLI cases are presented in figure 13(*b*,*d*). The impingement of the ramp shock on the cowl lip is evident near the top left-hand corners of the $\boldsymbol{u} \cdot \boldsymbol{\nabla} p$ contour plots. Such a shock at lip condition ensures maximum mass flow capture with optimum total pressure recovery (Seddon & Goldsmith 1999). The region of this computational boundary modelled as the no-slip wall is highlighted in black. The flow features are marked with respective numbers for clarity. The impinging cowl shock ① leads to boundary layer separation on the ramp surface of the baseline faceted case (figure 13*b*). The dividing

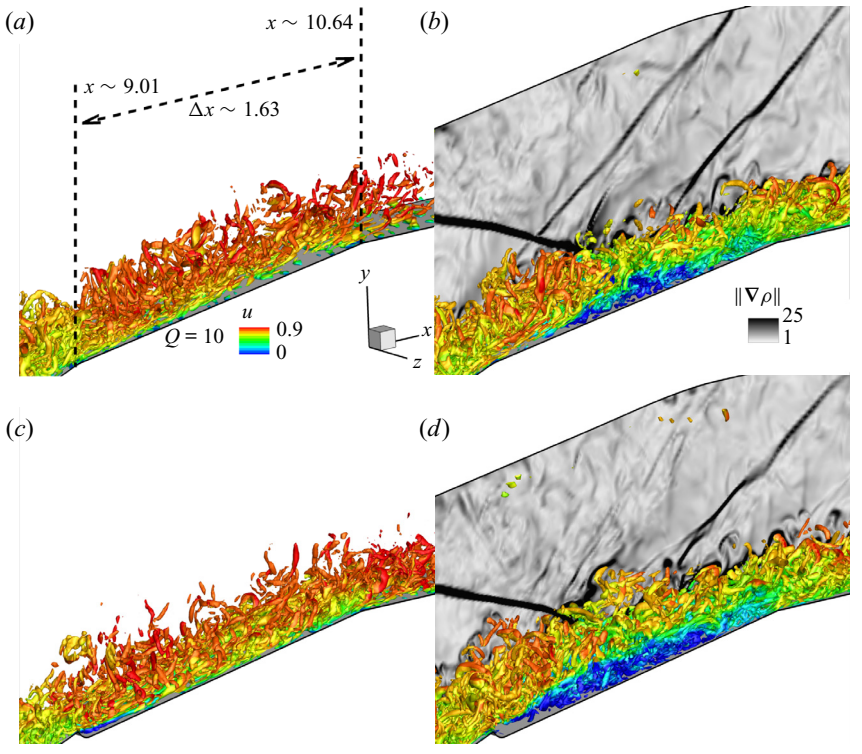

Figure 12. Flow structures identified using isolevel of Q-criterion, coloured with u-velocity: (*a*) ROC and (*b*) cowl SBLI for the faceted geometry. Panels (*c*,*d*) are the corresponding results for the notched geometry. Impinging and reflected shocks in the interaction region are visualized using density gradient magnitude ($\|\nabla\rho\|$) in (*b*,*d*).

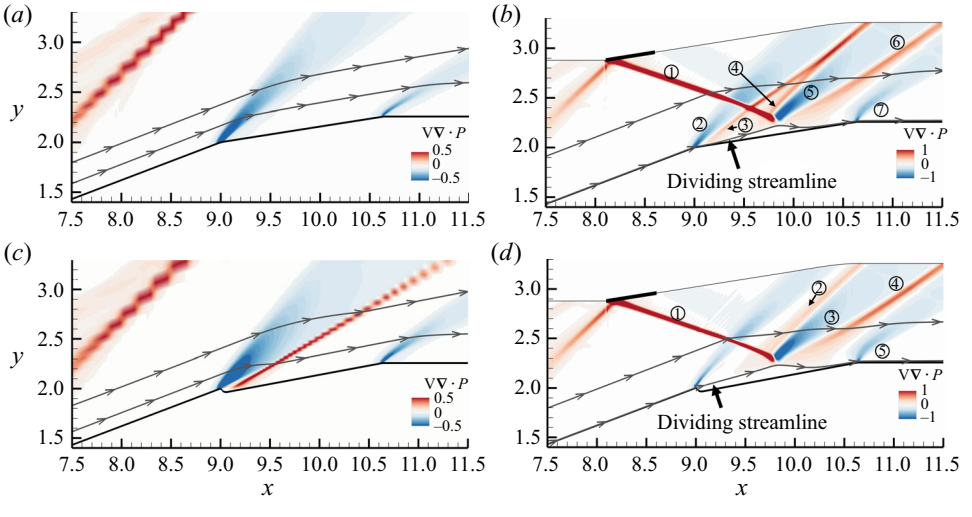

Figure 13. The $\boldsymbol{u}\cdot\nabla p$ fields of all four cases: (*a*) ROC and (*b*) cowl SBLI for the faceted geometry. Panels (*c*,*d*) are the corresponding results for the notched geometry. Streamlines are also indicated, including the dividing streamlines for the SBLI cases. Important flow features are marked with numbers for SBLI cases.

streamline indicates the extent of the separation bubble, which has a length of $0.903H_I$. The upstream end of the bubble is well-removed from the impinging cowl shock and creates a separation shock ③ and affects the expansion fan ②. The cowl shock continues downstream as a reflected shock ④, followed by an expansion fan ⑤ (created due to the decreasing thickness of the bubble). The separation shock and the reflected shock coalesce to form a single shock. A reattachment shock ⑥ also exists downstream of the expansion fan, where the separation bubble terminates. Finally, the flow encounters the expansion fan ⑦ at the isolator entrance. The interaction of the upstream expansion fan and the separated shock with the cowl shock leads to changes in respective wave angles. It has to be noted that the shocks and the expansion fans do not reflect back into the intake from the cowl-side wall at downstream locations due to the outflow conditions imposed there.

The SBLI over the notched junction (figure 13*d*) produces a larger separation bubble that originates from the step edge, and has a streamwise length of $1.141H_I$. Since control of SBLI is a major objective of junction design, the notch depth adopted here is approximately 31 % of the incoming boundary layer. Under this condition, the small separation bubble at the notch (discussed in figure 13*c*) coalesces with the elongated bubble generated by the impinging shock. For smaller notch depths, the edge bubble and the SBLI bubble remain separated, making the flow very similar to the baseline faceted case. Based on studies by Li & Liu (2019), it is important to have the impingement of the shock on the separated shear layer for effective control of SBLI. Comparing figure 13(*b*,*d*), it is evident that the notched junction eliminates the separation shock and significantly weakens the reflected shock ②. The cowl shock impinging on a separated shear layer reflects predominantly as an expansion fan ③. These features are consistent with the observations of Li & Liu (2019), based on the study of an idealized BFS. The reattachment shock ④ and the downstream expansion fan ⑤ are similar between the notched and the faceted cases.

The cowl SBLI cases are now compared with corresponding results from the experiments in figure 14. Qualitative comparisons are made between the experimental shadowgraphs (figure 14*a*,*c*) and the second derivatives of the mean DNS density fields (figure 14*b*,*d*).

Flow features are marked using arrows in the images for ease of comparison. A good agreement is observed between the two flow fields for both the faceted and the notched cases. The simulated expansion fan downstream of the reflected shock, and the reattachment shock, match with that from the experiments of the faceted geometry (figure 14*a*,*b*). The most prominent flow features of the notched junction (figure 14*c*,*d*) are the expansion fans (as a reflection of cowl shock) and the reattachment shocks, which again show a good match between the experiments and the DNS. The experiment identifies a relatively shorter separation bubble at the faceted junction, which starts slightly downstream from the corner. The differences in separation length scales can be attributed to the lower Reynolds number utilized in the DNS (e.g. the effect of Reynolds number as discussed in Lin & Pauley (1996)), as well as the three-dimensional effect in the experiments.

To quantitatively compare the flow fields from experiments and DNS, we provide wall-pressure plots in figure 15. Here, the spanwise and temporally averaged wall pressure from the DNS is compared with the temporally averaged centreline wall pressure measured on the intake floor. As the DNS was performed at $Re = 40\,000$, the wall pressure from RANS simulations performed at $Re = 400\,000$ is also included, to identify deviations in the high-fidelity simulations that are potentially driven by Reynolds number effects. In addition, to highlight the role of viscous effects, results from inviscid (Euler) simulations are also included.

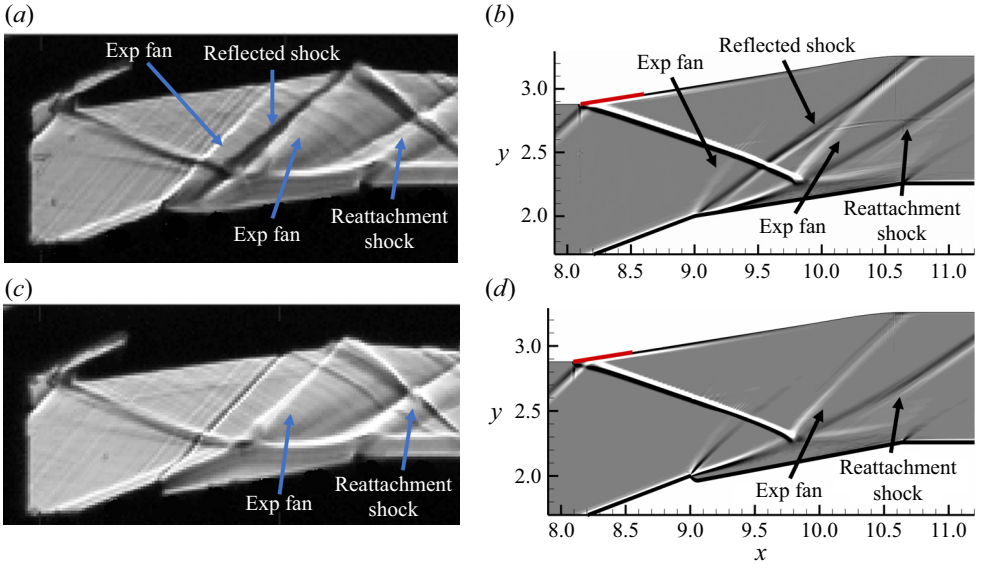

Figure 14. Comparison of Experimental and DNS shadowgraphs of SBLI flow fields: (*a*,*b*) faceted junction and (*c*,*d*) notched junction.

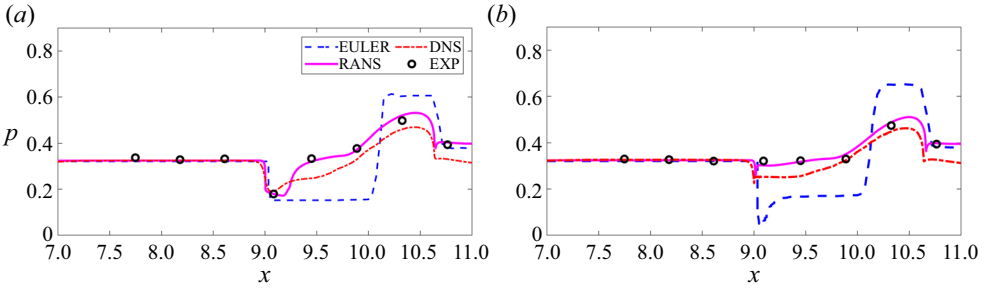

Figure 15. Comparison of experimental and DNS wall pressures: (*a*) faceted junction and (*b*) notched junction. Corresponding Euler and RANS simulations are also included.

All simulations display very close agreement with the experimental results over the ramp, upstream to the ramp–isolator junction ($x < 9$). Wall pressure at the faceted junction (figure 15*a*) drops at the corner due to the upstream expansion fan. In the inviscid simulation, wall pressure remains nearly constant ($9 \leq x \leq 10$) until the cowl shock impinges at the junction, which raises the wall pressure at $x \sim 10$. It further remains constant, until the expansion fan at the isolator entrance ($x \sim 10.6$) brings it down. The interaction between the cowl shock and the floor boundary layer is moderately strong in the present case, with viscous effects inducing flow separation. This causes the pressure distribution predicted by RANS simulations and DNS to be significantly different from that in the inviscid simulation. The general trends in the RANS and DNS predictions are consistent with those in the experiment. The mismatch between the DNS and experimental curves is attributed to the low-Reynolds number effect, which results in a relatively larger separation bubble in the DNS. This is further supported by the observation that the RANS simulation at the experimental Reynolds number rectifies this mismatch and closely follows the experimental measurements at all locations, both within and outside

the interaction region. The initial rise in wall-pressure ($9.3 < x < 10$) is due to the impinging/reflected shock, and the downstream pressure-rise ($10 < x < 10.7$) is induced by the reattachment shock. The downstream pressure drop through an expansion fan at the isolator entrance is visible in the viscous simulations as well.

In the case of the notched junction (figure 15*b*), viscous effects dominate at the ramp–isolator junction due to the flow separation induced by the step discontinuity. In supersonic BFS flows, prior studies have shown that the static pressure drops to lower levels in the base region due to expansion at the edge (Sfeir 1966), but the same was not observed in the present scenario. However, as typically observed in BFS flows (Sfeir 1966; Hartfield, Hollo & McDaniel 1993), the pressure is almost constant within the base region. The experimental and RANS pressure values at the junction continue to stay at almost the same level as the upstream flow, as there is only a marginal flow turning along the notch profile, which remains shielded from the outer inviscid flow by the bubble. The DNS pressure in the base region is lower than that in the experiments, but nonetheless, it follows the trend closely. Though a localized negative pressure gradient exists at the notch edge in the DNS, it does not propagate upstream, due to the turbulent nature of the incoming boundary layer (Sfeir 1966). Post reattachment, the pressure rises ($10 < x < 10.7$) due to the reattachment shock, and drops downstream due to the expansion fan at the isolator entrance.

4.2. *Dynamics of ramp–isolator junction*

To quantify the dynamics of the ramp–isolator junction, we extract the PSD from wall-pressure fluctuations for the ROC and SBLI cases. Figure 16(*a*,*c*) show spectra of the ROC, while figure 16(*b*,*d*) contain spectra with the cowl SBLI. The logarithms of the PSD values are plotted in order to ensure clarity of the trends. The ramp flows in all four cases exhibit similar dynamics involving KH instabilities and subsequent transition to turbulence at $x \sim 6.5$, which is marked using the vertical dashed lines. However, each flow harbours distinct dynamics downstream of the ramp–isolator junction, depending on the geometry and characteristics of the SBLI. The faceted ROC displays mitigation of unsteadiness each time the flow expands (at the junction and the isolator entrance). As the flow accelerates through the expansion fan, it tends to relaminarize (Narasimha & Sreenivasan 1973), resulting in a monotonic drop in PSD amplitudes. On the other hand, the notched ROC spectra first show a drop in unsteadiness at the upstream edge, followed by a peak and a decay as seen in figure 16(*c*), highlighted by an oval. This behaviour of the notched ROC is typical to BFS flows, where the oscillations peak immediately upstream of the reattachment, followed by a rapid decay (Eaton & Johnston 1981). There is a subsequent drop in unsteadiness over the isolator floor due to the effect of the downstream expansion fan. In both the ROC, the flow enters the isolator floor with diminished unsteadiness, which is outside the range of levels plotted here.

As seen in figure 16(*b*,*d*), the flow upstream of the ramp–isolator junction for the SBLI cases is nominally similar in dynamics to the ROC cases discussed above. However, the boundary layer interactions with the cowl shock energize a broad spectral range. Unlike the ROC cases, unsteadiness generated at the junction largely persists into the isolator section, in spite of the attenuation due to the downstream expansion fan.

The dynamics of the ramp–isolator junctions with cowl SBLI are further evaluated in detail, in the context of near-wall flow features. These wall-pressure spectra are aligned with the corresponding numerical shadowgraphs in figure 17. To juxtapose the unsteady scales in the interaction regions with SBLI literature, we adopt the separation length in the

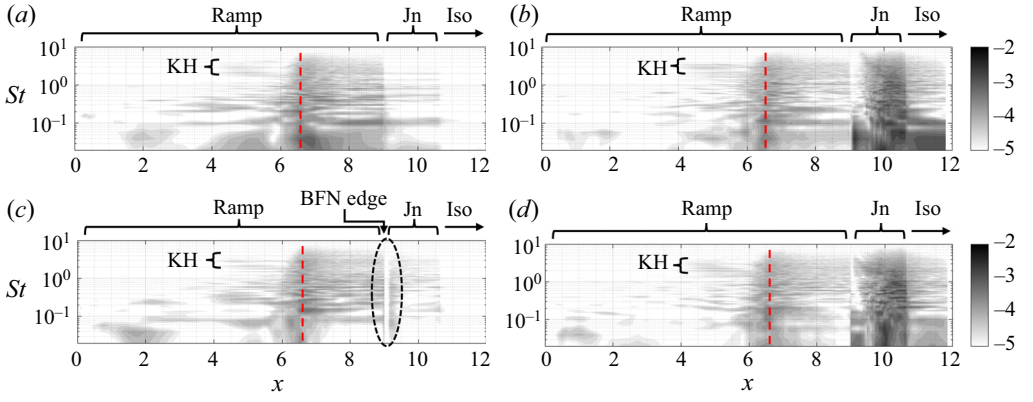

Figure 16. Wall pressure spectra (log–PSD) of the ramp, junction and isolator flow fields: (*a*) faceted ramp only; (*b*) faceted ramp SBLI; (*c*) notched ramp only; and (*d*) notched ramp SBLI. The red dashed lines indicate the transition to turbulence.

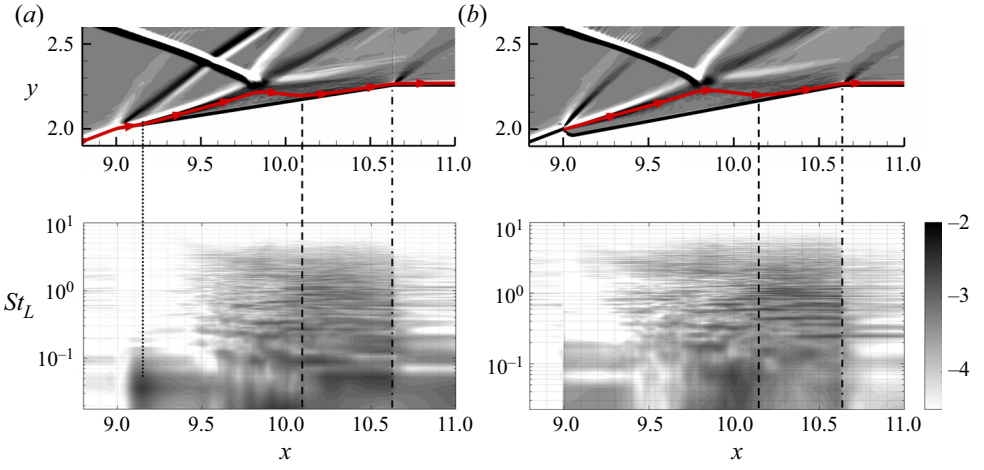

Figure 17. Wall pressure spectra (log–PSD) of junction SBLI: (*a*) Faceted and (*b*) Notched. Corresponding numerical shadowgraphs are also included for reference. The dotted line indicates the low-frequency peak in the faceted junction spectra. The dashed lines mark the reattachment locations. The dot-dashed lines mark the isolator start.

respective cases to scale the spectra. The dividing streamlines are also marked to indicate the boundaries of the separation bubbles.

A prominent feature of the faceted junction spectra (figure 17*a*) is the low-frequency peak ($St_L = 0.03$–0.04) near the separation and the reattachment points. It corresponds to the shock motion related to bubble breathing and matches very well with the spectral estimates in previous studies (Touber & Sandham 2009; Aubard *et al.* 2013). Since the separation bubble is relatively thinner in the faceted junction, the separated shear layer develops in close proximity to the wall surface. Therefore, the higher frequencies corresponding to shear layer instabilities ($St_L > 0.1$) are not excited until it is sufficiently thick ($x > 9.5$). The midfrequency component ($0.1 \leq St_L \leq 1$) corresponding to coherent fluctuations in the shear layer become prominent from $x \sim 9.5$. This has been attributed to KH instabilities that develop in the postinteraction shear layer of the bubble (Adler *et al.* 2018). The interaction region of the cowl shock also generates fine-scale structures that

populate the high-frequency content ($St_L > 1$). The drop in PSD amplitudes from the mid- to the high-frequency zone is consistent with the cascading effect. The bubble motion, KH instabilities of the shear layer, and the fine-scale structures contribute to the broadband content postreattachment ($10.1 \leq x \leq 10.6$). The attenuation effect of the expansion fan at the isolator entrance is most visible at higher frequencies, resulting in the dominance of low/low-midfrequency content ($St_L \leq 0.4$) within the isolator boundary layer.

The wall-pressure spectrum of the notched junction (figure 17*b*) exhibits a different set of dynamics. The prominent low-frequency peak related to bubble breathing is absent near the separation point. Here, flow separation is initiated at the upstream geometric discontinuity of the notch, which effectively locks the streamwise movement of the separation point. The reattachment point is still free to move, and hence the low-frequency content is visible at this location. The separated shear layer originating from the notch edge thickens and amplifies instabilities relatively quickly. The corresponding high-frequency oscillations ($St_L > 1$) emerge close to the notch-edge, followed by the midfrequency content ($0.1 \leq St_L \leq 1$). Post reattachment ($10.2 \leq x \leq 10.6$), the midfrequency content dominates, while the low-frequency oscillations become weaker, compared with the faceted junction, where this trend was reversed. This suggests the dominance of shear layer dynamics driven by shedding from the separation bubble. The trend continues into the isolator, which primarily retains a selective band of midfrequency oscillations ($0.2 \leq St_L \leq 0.4$). The current analysis reveals that utilizing a notched junction enforces one-sided locking of the separation bubble movement, thereby almost eliminating the low-frequency oscillations near the separation point, and significantly attenuating those within the isolator.

To quantify the effects of junction geometry on the unsteadiness of inviscid features of the compression path, the root mean squared (r.m.s.) values of pressure fluctuations from the DNS are presented in figure 18. The r.m.s. contours extracted from the midspan plane (figure 18*a*,*b*) identify several regions of unsteadiness, including the compression wave from the external ramp surface directed towards the cowl lip. High levels of fluctuations exist near the shock waves, including in the inviscid regions and regions of interaction with the boundary layer, and the flow downstream of the reattachment. Near-wall fluctuations attenuate at the isolator entrance due to the expansion fan, but the unsteadiness in the reattachment shock sustains. Among the shocked regions, peak unsteadiness is visible in the cowl shock, in relation to the separation shock and the reattachment shock. The separation shock fluctuations are primarily driven by the low-frequency motion of the separation bubble at the faceted junction, and this component is eliminated in the notched junction, consistent with the spectral analysis discussed in figure 17. The reattachment shock oscillations have additional contributions from shear layer structures and turbulent fluctuations. To compare the unsteadiness between the two junctions, the r.m.s. pressures are extracted along the common midstream line (marked using solid lines in figure 18*a*,*b*) and plotted in figure 18(*c*). The flow unsteadiness upstream to the junction shows a hump near the compression ramp shock at $x \sim 7.5$. A good match of r.m.s. values indicates that the incoming flows of both junctions are identical, as expected. The largest peaks are observed near the cowl shock in both geometries. However, the cowl shock of the faceted junction has comparatively higher unsteadiness. Downstream of the cowl shock, relatively smaller peaks represent the separation shock, expansion fans and reattachment shocks.

Additional r.m.s. traces are reported in figure 19 for both geometries, aligned with the corresponding mean $\boldsymbol{u} \cdot \nabla p$ fields. For the faceted junction, these are shown in figure 19(*a*). The peak r.m.s. value drops from trace F1 to F2 due to the interaction of the impinging cowl shock with the expansion fan. Such interaction of the impinging shock is absent in typical

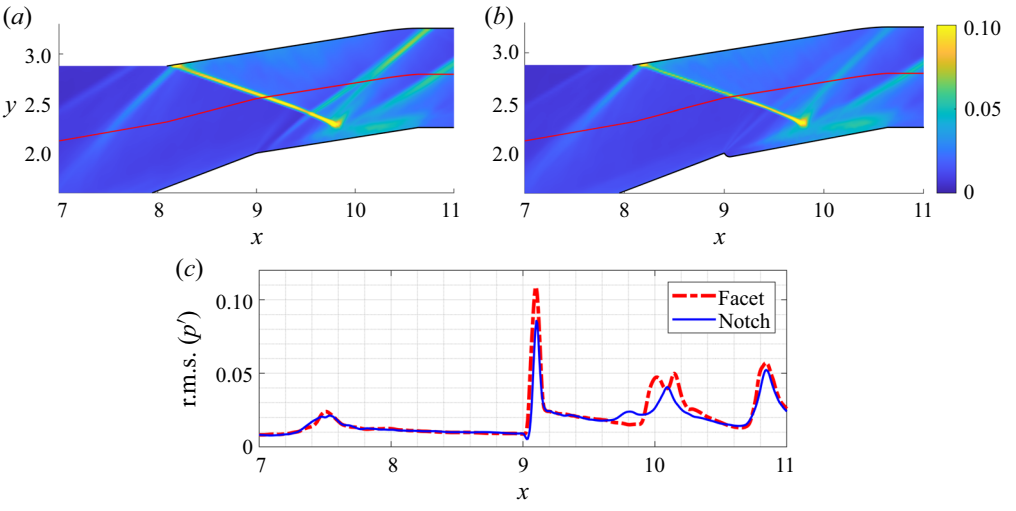

Figure 18. The r.m.s. pressures of the ramp–isolator junction flow fields: (*a*) faceted; (*b*) notched; (*c*) comparison along the domain centreline. The red line indicates probe points for comparison.

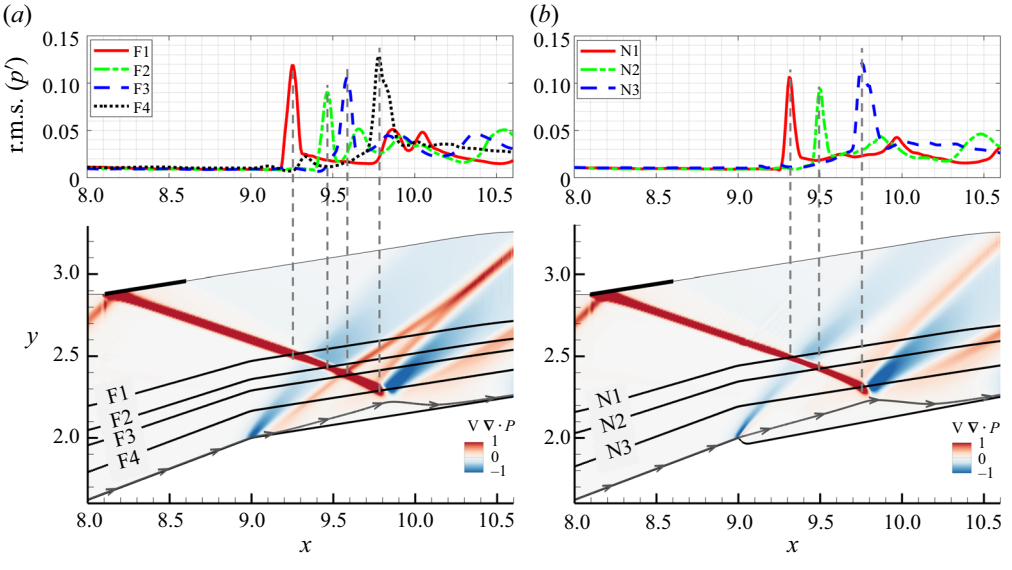

Figure 19. The r.m.s. pressures along the traces of (*a*) faceted and (*b*) notched junction. The $\boldsymbol{u} \cdot \nabla p$ fields aligned with the corresponding r.m.s. pressure distributions are also shown.

SBLI studies. The peak value increases again (trace F3) where the cowl shock interacts with the separation shock. The r.m.s. pressure peak is highest along trace F4 where the cowl shock interacts with the floor boundary layer. Similarly, around the notched junction (figure 19*b*), the peak r.m.s. pressure drops from trace N1 to N2 due to the interaction with the expansion fan originating at the edge of the notch. The cowl shock unsteadiness rises downstream and is highest near the interaction region (trace N3), close to the maximum thickness of the bubble.

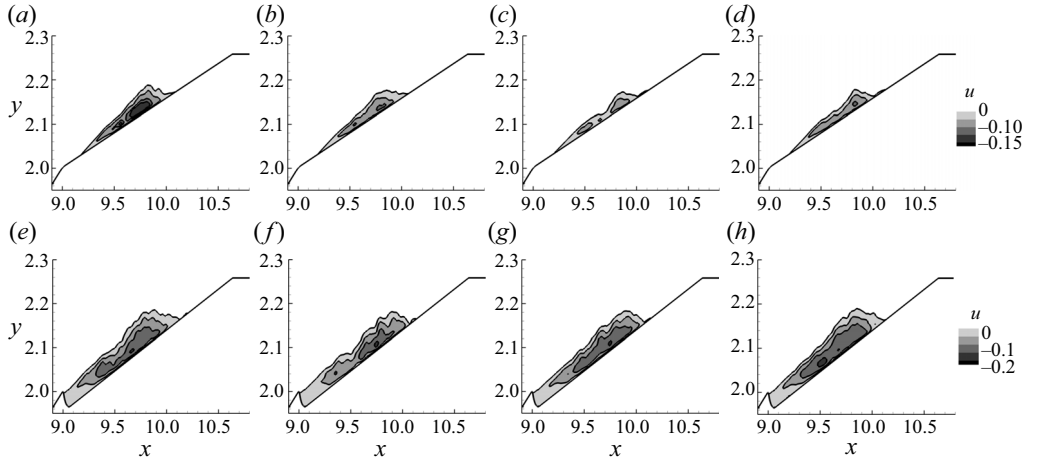

Figure 20. Contours of the low-frequency DMD modes in the (*a–d*) faceted and (*e–h*) notched junctions shown at equally spaced phase-intervals. The modes correspond to $St_L = 0.041$ and $St_L = 0.081$ for the faceted and notched cases, respectively. The mean flow field is added to the fluctuations. Here (*a*) $\phi = 0$; (*b*) $\phi = \pi/2$; (*c*) $\phi = \pi$; (*d*) $\phi = 3\pi/2$; (*e*) $\phi = 0$; (*f*) $\phi = \pi/2$; (*g*) $\phi = \pi$; (*h*) $\phi = 3\pi/2$.

To obtain the spatiotemporal forms of the unsteady features identified in wall spectra, we extract the relevant harmonics using DMD, from the streamwise velocity fluctuations on the midspan plane. Three modes are discussed in detail for each junction geometry, that are representative of the low-, mid- and high-frequency bands identified in figure 17.

The low-frequency mode is shown first in figure 20. The mean field is also added to the corresponding fluctuations to visualize the bubble-breathing motion that this mode represents. The bubble in the faceted junction is at its largest size in figure 20(*a*). The bubble shrinks as it sheds mass into the downstream flow, with the smallest size in figure 20(*c*). Subsequent entertainment of mass, and bubble dilation, are seen in figure 20(*d*). This breathing behaviour has been observed in experiments (Piponniau *et al.* 2009) and numerical simulations (Aubard *et al.* 2013) of canonical flat plate boundary layers with shock-induced separation. As shown by Piponniau *et al.* (2009), the streamwise movements of the bubble are linked with its contractions and dilatations in case of canonical impinging SBLI. The change in bubble size is a result of mass, momentum and vorticity transfer between the recirculating region and the outside flow. The mixing layer entrainment also plays an important role in this process.

The low-frequency behaviour at the notched junction is considerably different from that in the faceted junction, and is shown in figure 20(*e–h*). The breathing motion still exists, as the entrainment mechanism is active. However, in notched geometry, it primarily affects the downstream portion of the bubble at $x \sim 10$, consistent with the observations in the wall spectra (figure 17*b*). The dilation-phase of the bubble in this case is from $\phi = \pi/2$ to $\phi = 3\pi/2$. As the notch effectively locks the separation, the separation point has no effect of breathing motions. However, the reattachment point is influenced by bubble breathing, with its most upstream location corresponding to the smallest bubble size, and *vice versa*. The impact of bubble-breathing on variations in its streamwise location will be further evaluated in the context of separation and reattachment locations, later in this discussion.

The midfrequency modes for both geometries are shown in figure 21, along with the binary $\boldsymbol{u} \cdot \nabla p$ fields superimposed to indicate the mean states of cowl shock and dividing streamline. Figure 21(*a–d*) clearly show the shedding of structures from the shear layer,

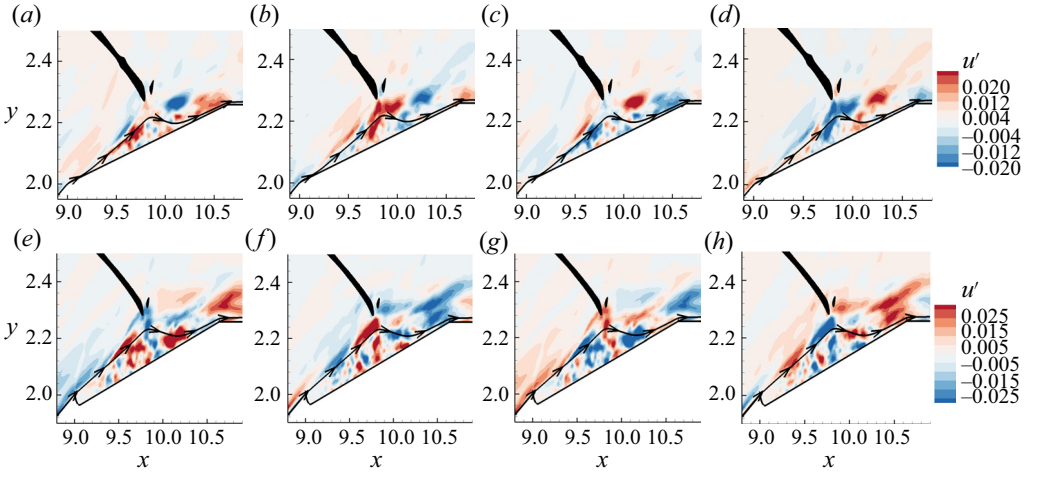

Figure 21. Contours of the midfrequency DMD modes in the (*a–d*) faceted and (*e–h*) notched junctions shown at equally spaced phase-intervals. The modes correspond to $St_L = 0.526$ and $St_L = 0.395$ for the faceted and notched cases, respectively. The mean states of the corresponding cowl shocks and dividing streamlines are also indicated. Here (*a*) $\phi = 0$; (*b*) $\phi = \pi/2$; (*c*) $\phi = \pi$; (*d*) $\phi = 3\pi/2$; (*e*) $\phi = 0$; (*f*) $\phi = \pi/2$, (*g*) $\phi = \pi$; (*h*) $\phi = 3\pi/2$.

which confirms their contribution to the midfrequency band of the faceted junction. The shedding results from KH instability waves, which are typically observed around laminar separation bubbles (e.g. Simoni *et al.* 2017; Rodríguez *et al.* 2018). The structures convect downstream and are attenuated across the expansion fan at the isolator corner. The midfrequency mode in the notched junction (figure 21*e–h*) has a different spatial form, with the shed vortical structures being relatively distorted. Since the shear layer originating from the notch's edge is well-developed, the notched junction has similarities with typical shock–shear layer interactions. For example, such 'distorting' vortical structures were observed by Karthick (2021) in a supersonic cavity shear layer, interacting with an impinging shock. The oscillations amplify after the shedding, and convect downstream into the isolator with strong amplitudes, even after passing through the expansion fan. This justifies the presence of a strong midfrequency component in the wall-pressure spectrum of the notched junction (figure 17*b*).

Corresponding results for the high-frequency modes are shown in figure 22. The high-frequency mode of the faceted junction (figure 22*a–d*) identifies the growth of vortical structures within the shear layer, from the separation point to the shock-impingement location. The PSD contours (shown earlier in figure 17*a*) also confirm the amplification of unsteadiness at medium and high-frequencies in this region ($x \sim 9.5$). Post interaction with the shock, the amplified structures disintegrate within the adverse-pressure gradient region, contributing to the fine-scale turbulence generated at the isolator entrance. The high-frequency mode of the notched junction (figure 22*e–h*) is very similar to that of the faceted junction. The similarity between these modes suggests the universality of fine-scale spatiotemporal scales in SBLI, in spite of differences in the thickness of the mean shear layers, and their relative displacements from the wall.

A quantitative comparison of the effects of various frequency bands on separation bubble dynamics is presented in figure 23. The displacement of the point of separation from its time-averaged position is shown in figure 23(*a*) for both geometries. Results are included for the three bands of frequencies discussed above. Corresponding results

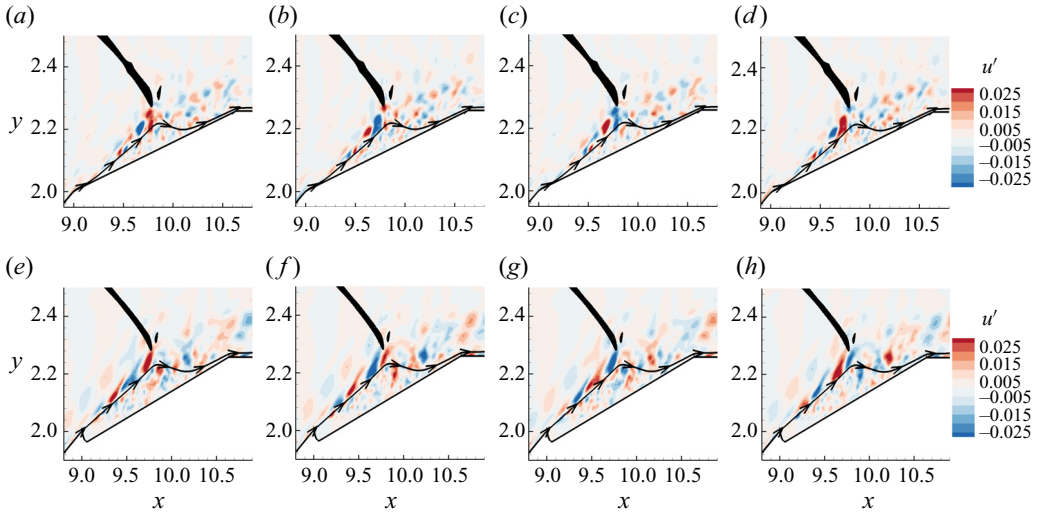

Figure 22. Contours of the high-frequency DMD modes in the (*a–d*) faceted and (*e–h*) notched junctions shown at equally spaced phase-intervals. The modes correspond to $St_L = 2.03$ and $St_L = 1.95$ for the faceted and notched cases, respectively. The mean states of the corresponding cowl shocks and dividing streamlines are also indicated. Here (*a*) $\phi = 0$; (*b*) $\phi = \pi/2$; (*c*) $\phi = \pi$; (*d*) $\phi = 3\pi/2$; (*e*) $\phi = 0$; (*f*) $\phi = \pi/2$; (*g*) $\phi = \pi$; (*h*) $\phi = 3\pi/2$.

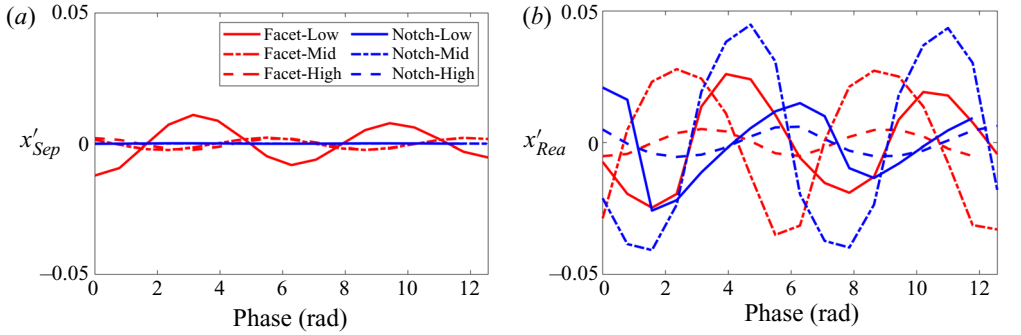

Figure 23. Comparison of streamwise oscillations of (*a*) separation point and (*b*) reattachment point caused by various bands of frequencies in the faceted and notched junctions.

for the reattachment location are plotted in figure 23(*b*). It is evident from figure 23(*a*) that the separation point in the notched junction experiences negligible fluctuations for all bands of frequencies, compared with that in the faceted junction. In the faceted junction, peak oscillations of the separation point are induced by the low-frequency component. Corresponding mid- and high-frequency oscillations are lower by an order of magnitude. This is because the upstream portion of the bubble harbours a nascent shear layer in which the associated instabilities have not amplified yet, compared with downstream locations.

The reattachment point has relatively amplified unsteadiness as seen in figure 23(*b*), for all bands of frequencies. While the high-frequency dynamics still have the lowest amplitudes, the low and midfrequency dynamics have comparable effects. An interesting observation here is that the midfrequency oscillations have higher amplitudes than the low-frequency oscillations in both geometries, indicating the significance of shear layer structures in impacting SBLI in inlets. The relative dominance of midfrequency

oscillations (of the reattachment point) over other frequency bands is most evident in the notched junction. The spatial form of this mode (figure 21*e–h*) had earlier identified these enhanced midfrequency oscillations to cause the shedding of vortical structures that persist in the isolator. This phenomenon could energize the boundary layer through cross-stream mixing of near-wall flow, assisting an efficient compression process. Unlike the separation point, the reattachment point oscillations of the faceted and notched junctions have similar amplitudes at low-frequency. However, their qualitative nature is different. The faceted junction displays symmetric bubble oscillations, whereas those in the notched geometry are asymmetric with relatively longer periods of bubble dilation, and a rapid contraction.

5. Effect on isolator flow

As seen in the above discussion, the geometry of the ramp–isolator junction has a significant effect on the dynamics of the boundary layer entering the isolator. Here we summarize the properties of the boundary layer on the ramp-side wall, to identify key variations in the flow at the leading end of the isolator. For this, flow properties are extracted on the ramp-side wall, and comparisons are made between the faceted and notched cases in figure 24. The selected probe locations at $x \sim 11.3$ are shown in figure 24(*a*) using the faceted geometry, overlaid with the $\boldsymbol{u} \cdot \boldsymbol{\nabla} p$ field. The Trettel–Larsson transformed mean streamwise velocity profiles are plotted in figure 24(*b*), which suggests a close match between the two cases. The linear relation between u^+_{TL} and y^+ is valid up to $y^+ \sim 7$, in the viscous sublayer. Farther from the wall, the profiles approach the log-layer reference line (approximately $20 \leq y^+ \leq 200$), eventually deviating from it, as explained by the law of the wake. The computed profiles are not expected to perfectly adhere to the turbulent profile. As shown by Pirozzoli & Grasso (2006), postinteraction boundary layers attain equilibrium turbulent characteristics only at significantly large distances downstream of the SBLI region.

The static pressure in the isolator has implications for combustion instabilities in the engine. Figure 24(*c*) compares the static pressure profiles in the isolator at $x \sim 11.3$. The notched geometry results in a lower static pressure within the isolator boundary layer due to the elimination of the separation shock. Consistent with this trend, the experimental studies also showed lower back-pressures at the end of the isolator, in the notched intake. This is a favourable flow modification since static pressure reduction is conducive to relaxation in structural loads. The stagnation pressure profiles in the isolator are shown in figure 24(*d*). While the total pressures of the notched intake are slightly lower (compared with the faceted intake) within the boundary layer, it increases in the inviscid region away from the wall. This is consistent with the thicker shear layer, and weaker separation shock of the notched geometry. A similar trend is seen in the Mach profiles at the start of the isolator (figure 24*e*).

Turbulent statistics of these boundary layers at $x \sim 11.3$ are summarized in figure 25. The r.m.s. profiles of fluctuations in various velocity components are plotted in figure 25(*a*), which are qualitatively similar to those presented by Wu & Moin (2009) and Duan *et al.* (2021) for supersonic flat plate boundary layers. While all fluctuations display similar behaviour in both the geometries near the wall ($y^+ \leq 7$), fluctuations attain higher amplitudes away from the wall in the notched geometry. Deviations first appear in the spanwise velocity fluctuations within the buffer layer ($y^+ > 7$), followed by wall-normal velocity fluctuations, which deviate from each other inside the log-layer, approximately at $y^+ > 30$. Finally, streamwise velocity fluctuations deviate in the outer regions of the log-layer, with $y^+ > 50$. These differences are primarily driven by the relatively intense shedding of vortical structures in the midfrequency band at the notched junction, which

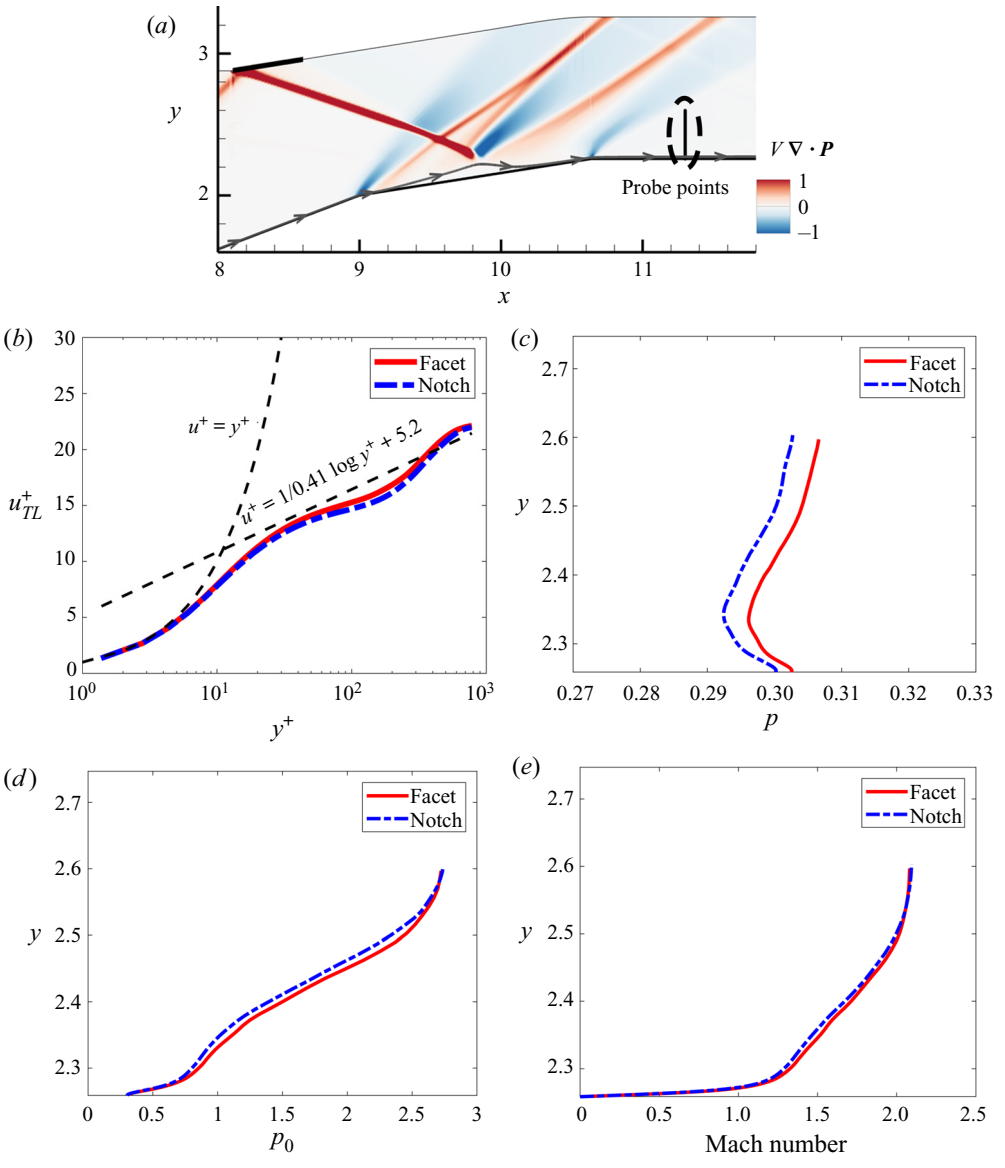

Figure 24. (*a*) The $\boldsymbol{u} \cdot \nabla P$ field with the probe points in the isolator. (*b*) Mean velocity profiles in inner scaling. (*c*) Static pressure profiles. (*d*) Stagnation pressure profiles. (*e*) Mach profiles.

leads to enhanced transverse mixing in the boundary layer. The cumulative effects of these fluctuations are visualized in the TKE plots in figure 25(*b*). The TKE values are higher in the buffer and log layers, for the notched geometry. The higher levels of TKE in the isolator result from the upstream shock–shear layer interaction (Shi *et al.* 2021), which is relatively dominant in the notched junction. Typical TKE distributions in zero pressure-gradient equilibrium boundary layers have a single peak in the boundary layer. However, flows with adverse pressure gradients exhibit a second (outer) peak, e.g. as discussed in Tanarro, Vinuesa & Schlatter (2020), due to higher turbulent stresses in the outer region of the

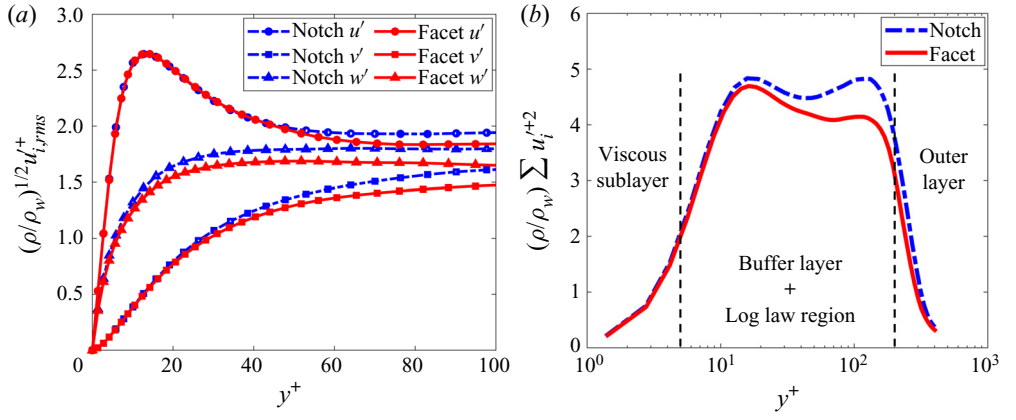

Figure 25. (*a*) The r.m.s. velocity fluctuation intensities and (*b*) turbulent kinetic energy distribution across the isolator boundary layer.

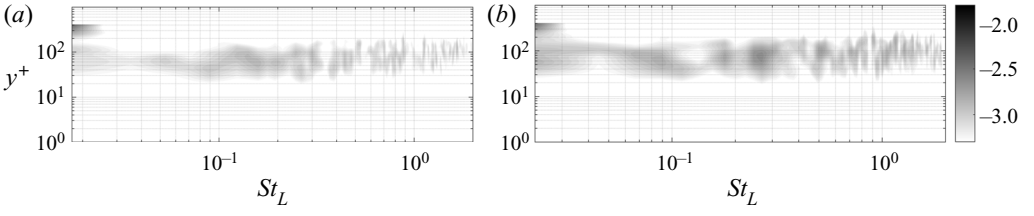

Figure 26. The Y-velocity spectra (log–PSD) of isolator boundary layer: (*a*) faceted and (*b*) notched.

boundary layer. Interestingly, the outer peak is revealed to be the relatively dominant feature of the notched geometry, highlighting the downstream impact of junction design.

The wall-normal velocity spectra of the isolator boundary layers at $x \sim 11.3$ are presented in figure 26. The dominant component of unsteadiness exists in the log-layer across all frequencies for both geometries, except for the low-frequency component, which is prominent in the outer region of the boundary layer. Although the notched spectrum in general shows higher amplitudes compared with the faceted spectrum, its most distinct feature is the midfrequency peak at $St_L \sim 0.27$. This further confirms the role of shear layer instabilities shed from the ramp–isolator junction in amplifying the unsteadiness in the notched boundary layer, as seen in figure 25(*b*).

Experimental studies support the above trends by inferring that the boundary layer near the end of the isolator duct is relatively fuller in the notched intake. This is evident in the Mach profiles shown in figure 27(*a*), which are obtained from total-pressure rake measurements at the end of the isolator duct ($x \sim 14.4$) in the experiments. The boundary layer energization also results in increased total pressures near the wall as displayed in figure 27(*b*). The higher total pressure recovery with a notch is conducive to improve the intake performance. The analysis of DNS data thus identifies the relatively more excited state of the isolator inflow in the notched intake. The enhanced midfrequency mechanisms due to the notched junction promote stronger mixing in the boundary layer and momentum transport to the near-wall regions. The fuller boundary layer also suggests improved flow uniformity, which aids effective combustion, after the flow enters the combustor.

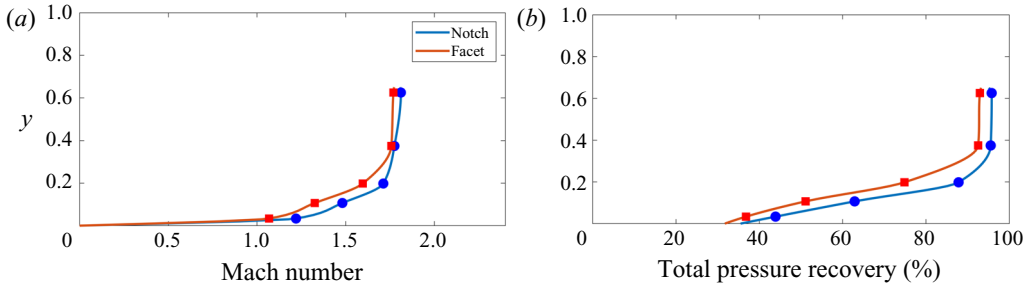

Figure 27. (*a*) Mach number and (*b*) total pressure recovery measured in the experiments at the end of the isolator.

6. Conclusions

Fundamental mechanisms affecting the external ramp flow and cowl SBLIs in a Mach 3 mixed compression intake are explored through a computational study and associated experimental data. The focus is on first understanding boundary layer transition and turbulence over the external compression ramp, followed by developing control strategies based on geometric modifications to improve the robustness of the ramp–isolator junction SBLI. Based on feasibility constraints, the DNS are performed at a Reynolds number of an order of magnitude lower than the corresponding experiments. The RANS simulations at the experimental *Re* and inviscid Euler simulations are also utilized to address the impact of this choice on computed flow fields.

A three-dimensional linear global analysis identifies temporally damped shear layer modes corresponding to KH instabilities over the separation bubble on the external ramp. The least-damped KH modes exhibit a two-dimensional nature and persist downstream of the bubble-reattachment location. The ramp bubble also sustains an absolute instability in the form of a three-dimensional stationary mode, which is captured in the DNS flow field as a low-frequency harmonic near the wall. The nonlinear simulations identify the breakdown of this stationary mode due to secondary instabilities driven by the shear layer modes, which turbulizes the ramp boundary layer prior to entering the isolator.

The ramp–isolator junction flow is studied for two geometric configurations, including a faceted and a notched design. The ROC, as well as the cowl shock impingement scenario, are simulated to systematically address the flow complexities in the interaction region. The junction wall-pressure predictions from DNS and RANS closely match with the experimental data. The dynamics of the junction flow are interpreted in the context of the SBLI literature on the low-, mid- and high-frequency scales, usually observed in the interaction region. The faceted junction displays the typical behaviour of an impinging flat-plate SBLI, but some variations exist in the separation zone, due to the interaction of the upstream expansion fan with the cowl shock. On the other hand, the notched junction is reminiscent of a shock–shear layer interaction, which almost eliminates the reflected shock. The low-frequency unsteadiness corresponding to the bubble-breathing motion has a strong signature near the separation and reattachment locations of the faceted junction. The notched junction, however, locks the upstream extent of the bubble, thus attenuating the low-frequency oscillations at the separation location. The modal analysis identifies the shedding of vortical structures in the midfrequency range for both geometries. These frequencies are found to equally impact the reattachment location of the bubble, as the low-frequency component. Spectral and modal analyses suggest that midfrequency dynamics of the cowl SBLI are relatively predominant in the notched junction, and

corresponding vortical structures are distorted in relation to the faceted junction. While these shed vortical structures rapidly attenuate in the faceted geometry, they persist into the notched isolator.

The design of the junction also impacts the state of the turbulent boundary layer inside the isolator. Elimination of the separation shock in the notched junction reduces the intake static pressure and aids in the mitigation of structural loads. The increase in velocity fluctuations and TKE due to the notch promotes better cross-stream mixing near the wall, which is confirmed through higher energy content at midfrequencies in the log-layer of the notched isolator. The spatiotemporal dynamics and mechanisms revealed in the present study thus explain the existence of a fuller boundary layer profile in the notched intake, as measured in the corresponding experiments. The energizing effect of the notch could provide an effective passive control strategy, that improves the robustness and efficacy of high-speed propulsion systems, and make it better equipped to suppress or delay an unstart.

Funding. This research was partly supported by the Office of Naval Research (grant N00014-22-1-2005), monitored by D. Gonzalez. Computations were performed at the Research Computing Center, Florida State University.

Declaration of interests. The authors report no conflict of interest.

Author ORCIDs.
Nikhil Khobragade https://orcid.org/0000-0002-6153-0959.

References

Adams, N.A. 2000 Direct simulation of the turbulent boundary layer along a compression ramp at $M = 3$ and $Re\theta = 1685$. *J. Fluid Mech.* **420**, 47–83.

Adler, M.C., Gonzalez, D.R., Stack, C.M. & Gaitonde, D.V. 2018 Synthetic generation of equilibrium boundary layer turbulence from modeled statistics. *Comput. Fluids* **165**, 127–143.

Agostini, L., Larchevêque, L., Dupont, P., Debiève, J.-F. & Dussauge, J.-P. 2012 Zones of influence and shock motion in a shock/boundary-layer interaction. *AIAA J.* **50** (6), 1377–1387.

Alam, M. & Sandham, N.D. 2000 Direct numerical simulation of 'short' laminar separation bubbles with turbulent reattachment. *J. Fluid Mech.* **410**, 1–28.

Ali, M.Y., Alvi, F., Manisankar, C., Verma, S. & Venkatakrishnan, L. 2011 Studies on the control of shock wave-boundary layer interaction using steady microactuators. In *41st AIAA Fluid Dynamics Conference and Exhibit, AIAA Paper* 2011-3425.

Anderson, D., Tannehill, J. & Pletcher, R. 1984 *Computational Fluid Mechanics and Heat Transfer*. McGraw-Hill.

Aubard, G., Gloerfelt, X. & Robinet, J.-C. 2013 Large-eddy simulation of broadband unsteadiness in a shock/boundary-layer interaction. *AIAA J.* **51** (10), 2395–2409.

Bagheri, S., Åkervik, E., Brandt, L. & Henningson, D.S. 2009 Matrix-free methods for the stability and control of boundary layers. *AIAA J.* **47** (5), 1057–1068.

Balsara, D.S. & Shu, C.-W. 2000 Monotonicity preserving weighted essentially non-oscillatory schemes with increasingly high order of accuracy. *J. Comput. Phys.* **160** (2), 405–452.

Beam, R. & Warming, R. 1978 An implicit factored scheme for the compressible Navier–Stokes equations. *AIAA J.* **16** (4), 393–402.

Bhagatwala, A. & Lele, S.K. 2009 A modified artificial viscosity approach for compressible turbulence simulations. *J. Comput. Phys.* **228** (14), 4965–4969.

Caraballo, E., Webb, N., Little, J., Kim, J.-H. & Samimy, M. 2009 Supersonic inlet flow control using plasma actuators. In *47th AIAA Aerospace Sciences Meeting including the New Horizons Forum and Aerospace Exposition, AIAA Paper* 2009-924.

Cherubini, S., Robinet, J.-C., De Palma, P. & Alizard, F. 2010 The onset of three-dimensional centrifugal global modes and their nonlinear development in a recirculating flow over a flat surface. *Phys. Fluids* **22** (11), 114102.

De Vanna, F., Picano, F., Benini, E. & Quinn, M.K. 2021 Large-eddy simulations of the unsteady behaviour of a hypersonic intake at *m*ach 5. *AIAA J.* **59** (10), 1–14.

DÉLERY, J., MARVIN, J.G. & RESHOTKO, E. 1986 Shock-wave boundary layer interactions. *Tech. Rep.* Advisory Group for Aerospace Research and Development Neuilly-Sur-Seine (France).

DOLLING, D.S. 2001 Fifty years of shock-wave/boundary-layer interaction research: what next? *AIAA J.* **39** (8), 1517–1531.

DOLLING, D.S. & MURPHY, M.T. 1983 Unsteadiness of the separation shock wave structure in a supersonic compression ramp flowfield. *AIAA J.* **21** (12), 1628–1634.

DUAN, J., LI, X., LI, X. & LIU, H. 2021 Direct numerical simulation of a supersonic turbulent boundary layer over a compression–decompression corner. *Phys. Fluids* **33** (6), 065111.

DUPONT, P., PIPONNIAU, S., SIDORENKO, A. & DEBIÈVE, J.F. 2008 Investigation by particle image velocimetry measurements of oblique shock reflection with separation. *AIAA J.* **46** (6), 1365–1370.

EATON, J.K. & JOHNSTON, J.P. 1981 A review of research on subsonic turbulent flow reattachment. *AIAA J.* **19** (9), 1093–1100.

FLORYAN, J.M. 1991 On the Görtler instability of boundary layers. *Prog. Aerosp. Sci.* **28** (3), 235–271.

GAITONDE, D.V. 2015 Progress in shock wave/boundary layer interactions. *Prog. Aerosp. Sci.* **72**, 80–99.

GARMANN, D.J. 2013 Characterization of the vortex formation and evolution about a revolving wing using high-fidelity simulation. PhD thesis, University of Cincinnati.

GEROLYMOS, G.A. 1990 Implicit multiple-grid solution of the compressible Navier–Stokes equations using $k - \epsilon$ turbulence closure. *AIAA J.* **28** (10), 1707–1717.

HARTFIELD, R.J JR., Hollo, S.D. & McDaniel, J.C. 1993 Planar measurement technique for compressible flows using laser-induced iodine fluorescence. *AIAA J.* **31** (3), 483–490.

HILDEBRAND, N., DWIVEDI, A., NICHOLS, J.W., JOVANOVIĆ, M.R. & CANDLER, G.V. 2018 Simulation and stability analysis of oblique shock-wave/boundary-layer interactions at mach 5.92. *Phys. Rev. Fluids* **3** (1), 013906.

HOLDEN, H.A. & BABINSKY, H. 2005 Separated shock-boundary-layer interaction control using streamwise slots. *J. Aircraft* **42** (1), 166–171.

HOSSEINVERDI, S. & FASEL, H.F. 2019 Numerical investigation of laminar–turbulent transition in laminar separation bubbles: the effect of free-stream turbulence. *J. Fluid Mech.* **858**, 714–759.

HUERRE, P. & MONKEWITZ, P.A. 1985 Absolute and convective instabilities in free shear layers. *J. Fluid Mech.* **159**, 151–168.

HUNT, R.L. & GAMBA, M. 2019 On the origin and propagation of perturbations that cause shock train inherent unsteadiness. *J. Fluid Mech.* **861**, 815–859.

KARTHICK, S.K. 2021 Shock and shear layer interactions in a confined supersonic cavity flow. *Phys. Fluids* **33** (6), 066102.

KAUSHIK, M. 2019 Experimental studies on micro-vortex generator controlled shock/boundary-layer interactions in mach 2.2 intake. *Intl J. Aeronaut. Space Sci.* **20** (3), 584–595.

KHOBRAGADE, N., GUSTAVSSON, J., KUMAR, R., KIRBY, S., BIRCH, T.J., MAI, C.L. & TAYLOR, R.H. 2020 Characterization of bleedless shockwave boundary layer interaction control for high speed intakes. In *AIAA Scitech 2020 Forum, AIAA Paper* 2020-2091.

KHOBRAGADE, N., UNNIKRISHNAN, S. & KUMAR, R. 2021 Linear and nonlinear flow analysis of elements of a supersonic inlet. *AIAA J.* **59** (11), 4392–4409.

KRISHNAN, L., SANDHAM, N.D. & STEELANT, J. 2009 Shock-wave/boundary-layer interactions in a model scramjet intake. *AIAA J.* **47** (7), 1680–1691.

KUMAR, R., ALI, M.Y., ALVI, F.S. & VENKATAKRISHNAN, L. 2011 Generation and control of oblique shocks using microjets. *AIAA J.* **49** (12), 2751–2759.

KURELEK, J.W., LAMBERT, A.R. & YARUSEVYCH, S. 2016 Coherent structures in the transition process of a laminar separation bubble. *AIAA J.* **54** (8), 2295–2309.

VAN LEER, B. 1979 Towards the ultimate conservation difference scheme V, a second-order sequel to Godunov's method. *J. Comput. Phys.* **32**, 101–136.

LI, W. & LIU, H. 2019 Large-eddy simulation of shock-wave/boundary-layer interaction control using a backward facing step. *Aerosp. Sci. Technol.* **84**, 1011–1019.

LI, F. & MALIK, M.R. 1995 Fundamental and subharmonic secondary instabilities of Görtler vortices. *J. Fluid Mech.* **297**, 77–100.

LIN, J.C.M. & PAULEY, L.L. 1996 Low-Reynolds-number separation on an airfoil. *AIAA J.* **34** (8), 1570–1577.

LÜDEKE, H. & SANDHAM, N. 2010 Direct numerical simulation of the transition process in a separated supersonic ramp flow. In *40th Fluid Dynamics Conference and Exhibit, AIAA Paper* 2010-4470.

MORGAN, B., DURAISAMY, K. & LELE, S.K. 2014 Large-eddy simulations of a normal shock train in a constant-area isolator. *AIAA J.* **52** (3), 539–558.

NARASIMHA, R. & SREENIVASAN, K.R. 1973 Relaminarization in highly accelerated turbulent boundary layers. *J. Fluid Mech.* **61** (3), 417–447.

OSWATITSCH, K. 1980 Pressure recovery for missiles with reaction propulsion at high supersonic speeds (the efficiency of shock diffusers). In *Contributions to the Development of Gasdynamics*, pp. 290–323. Springer.

PAULEY, L.L., MOIN, P. & REYNOLDS, W.C. 1990 The structure of two-dimensional separation. *J. Fluid Mech.* **220**, 397–411.

PIPONNIAU, S., DUSSAUGE, J.-P., DEBIEVE, J.-F. & DUPONT, P. 2009 A simple model for low-frequency unsteadiness in shock-induced separation. *J. Fluid Mech.* **629**, 87–108.

PIROZZOLI, S. & GRASSO, F. 2006 Direct numerical simulation of impinging shock wave/turbulent boundary layer interaction at $M = 2.25$. *Phys. Fluids* **18** (6), 065113.

PRIEBE, S. & MARTÍN, M.P. 2012 Low-frequency unsteadiness in shock wave–turbulent boundary layer interaction. *J. Fluid Mech.* **699**, 1–49.

PULLIAM, T.H. & CHAUSSEE, D.S. 1981 A diagonal form of an implicit approximate-factorization algorithm. *J. Comput. Phys.* **39** (2), 347–363.

RANJAN, R., UNNIKRISHNAN, S. & GAITONDE, D. 2020 A robust approach for stability analysis of complex flows using high-order Navier–Stokes solvers. *J. Comput. Phys.* **403**, 109076.

RANJAN, R., UNNIKRISHNAN, S., ROBINET, J.-C. & GAITONDE, D. 2021 Global transition dynamics of flow in a lid-driven cubical cavity. *Theor. Comput. Fluid Dyn.* **35** (3), 397–418.

RIZZETTA, D.P. & VISBAL, M.R. 1993 Comparative numerical study of two turbulence models for airfoil static and dynamic stall. *AIAA J.* **31** (4), 784–786.

RODRIGUEZ, D. & THEOFILIS, V. 2010 Structural changes of laminar separation bubbles induced by global linear instability. *J. Fluid Mech.* **655**, 280–305.

RODRÍGUEZ, D., GENNARO, E.M. & SOUZA, L.F. 2018 Self-excited primary and secondary instability of laminar separation bubbles. *J. Fluid Mech.* **906**, A13.

ROE, P.L. 1981 Approximate Riemann solvers, parameter vectors and difference schemes. *J. Comput. Phys.* **43**, 357–372.

SCHMID, P.J. 2010 Dynamic mode decomposition of numerical and experimental data. *J. Fluid Mech.* **656**, 5–28.

SEDDON, J. & GOLDSMITH, E.L. 1999 *Intake Aerodynamics*, vol. 2. Blackwell Science Boston.

SFEIR, A. 1966 Supersonic flow separation on a backward facing step. *Tech. Rep.* California Univ Berkeley Div of Aeronautical Sciences.

SHI, F., GAO, Z., JIANG, C. & LEE, C.-H. 2021 Numerical investigation of shock-turbulent mixing layer interaction and shock-associated noise. *Phys. Fluids* **33** (2), 025105.

SHU, C.W. & OSHER, S. 1988 Efficient implementation of essentially non-oscillatory shock-capturing schemes. *J. Comput. Phys.* **77** (2), 439–471.

SIMONI, D., LENGANI, D., UBALDI, M., ZUNINO, P. & DELLACASAGRANDE, M. 2017 Inspection of the dynamic properties of laminar separation bubbles: free-stream turbulence intensity effects for different Reynolds numbers. *Exp. Fluids* **58** (6), 66.

SOUVEREIN, L.J., DUPONT, P., DEBIEVE, J.-F., DUSSAUGE, J.-P., VAN OUDHEUSDEN, B.W. & SCARANO, F. 2010 Effect of interaction strength on unsteadiness in shock-wave-induced separations. *AIAA J.* **48** (7), 1480–1493.

TANARRO, Á., VINUESA, R. & SCHLATTER, P. 2020 Effect of adverse pressure gradients on turbulent wing boundary layers. *J. Fluid Mech.* **883**, A8.

TERAMOTO, S. 2005 Large-eddy simulation of transitional boundary layer with impinging shock wave. *AIAA J.* **43** (11), 2354–2363.

THEOFILIS, V., HEIN, S. & DALLMANN, U. 2000 On the origins of unsteadiness and three-dimensionality in a laminar separation bubble. *Phil. Trans. R. Soc. Lond.* A **358** (1777), 3229–3246.

TONG, F., LI, X., DUAN, Y. & YU, C. 2017 Direct numerical simulation of supersonic turbulent boundary layer subjected to a curved compression ramp. *Phys. Fluids* **29** (12), 125101.

TOUBER, E. & SANDHAM, N.D. 2009 Large-eddy simulation of low-frequency unsteadiness in a turbulent shock-induced separation bubble. *Theor. Comput. Fluid Dyn.* **23** (2), 79–107.

TRETTEL, A. & LARSSON, J. 2016 Mean velocity scaling for compressible wall turbulence with heat transfer. *Phys. Fluids* **28** (2), 026102.

UNNIKRISHNAN, S. & GAITONDE, D.V. 2020 Linear, nonlinear and transitional regimes of second-mode instability. *J. Fluid Mech.* **905**, A25.

UNNIKRISHNAN, S. & GAITONDE, D.V. 2021 Perturbation analysis of nonlinear stages in hypersonic transition. *Intl J. Comput. Fluid Dyn.* **35** (5), 306–318.

VALDIVIA, A., YUCEIL, K.B., WAGNER, J.L., CLEMENS, N.T. & DOLLING, D.S. 2014 Control of supersonic inlet-isolator unstart using active and passive vortex generators. *AIAA J.* **52** (6), 1207–1218.

VERMA, S.B. & MANISANKAR, C. 2012 Shockwave/boundary-layer interaction control on a compression ramp using steady micro jets. *AIAA J.* **50** (12), 2753–2764.

VINOKUR, M. 1974 Conservation equations of gasdynamics in curvilinear coordinate systems. *J. Comput. Phys.* **14** (2), 105–125.

VISBAL, M. & GAITONDE, D. 1998 High-order accurate methods for unsteady vortical flows on curvilinear meshes. In *36th AIAA Aerospace Sciences Meeting and Exhibit, AIAA Paper* 1998-0131.

WAGNER, J.L., YUCEIL, K.B., VALDIVIA, A., CLEMENS, N.T. & DOLLING, D.S. 2009 Experimental investigation of unstart in an inlet/isolator model in mach 5 flow. *AIAA J.* **47** (6), 1528–1542.

WATMUFF, J.H. 1999 Evolution of a wave packet into vortex loops in a laminar separation bubble. *J. Fluid Mech.* **397**, 119–169.

WEBB, N., CLIFFORD, C. & SAMIMY, M. 2013 An investigation of the control mechanism of plasma actuators in a shock wave-boundary layer interaction. In *51st AIAA Aerospace Sciences Meeting including the New Horizons Forum and Aerospace Exposition, AIAA Paper* 2013-402.

WU, X. & MOIN, P. 2009 Direct numerical simulation of turbulence in a nominally zero-pressure-gradient flat-plate boundary layer. *J. Fluid Mech.* **630**, 5–41.

YAO, Y., KRISHNAN, L., SANDHAM, N.D. & ROBERTS, G.T. 2007 The effect of mach number on unstable disturbances in shock/boundary-layer interactions. *Phys. Fluids* **19** (5), 054104.

ZHANG, K., SANDHAM, N.D. & HU, Z. 2018 Instability of supersonic ramp flow with intermittent transition to turbulence. In *Direct and Large-Eddy Simulation X*, pp. 373–378. Springer.

ZHANG, Y., TAN, H., SUN, S. & RAO, C. 2015 Control of cowl shock/boundary-layer interaction in hypersonic inlets by bump. *AIAA J.* **53** (11), 3492–3496.

ZHANG, Y., TAN, H., ZHUANG, Y. & WANG, D. 2014 Influence of expansion waves on cowl shock/boundary layer interaction in hypersonic inlets. *J. Propul. Power* **30** (5), 1183–1191.